Probing surface plasmons with optical emitters

E. Verhagen

Supervised by Prof. Dr. A. Polman

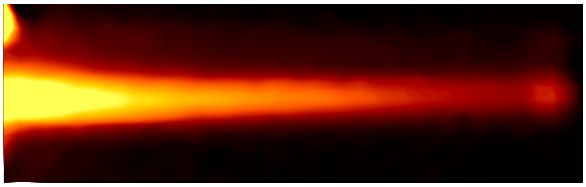

Report of a research project for the masters degree
in experimental physics of Utrecht University
performed in the period August 2004 - August 2005

at

Center for Nanophotonics
FOM-institute for Atomic and Molecular Physics
Kruislaan 407, 1098 SJ Amsterdam, The Netherlands

Abstract

Surface plasmons propagating at metal/dielectric interfaces provide a possible route towards the miniaturization and integration of optical components. In this work, we study the excitation, propagation and damping of surface plasmons experimentally in the visible and infrared. Calculations of the dispersion and damping of surface plasmon modes in multilayer geometries and on lamellar gratings are presented.

In the visible, surface plasmons excited by focussing 532 nm light through an objective on grooves and microgratings in Ag films are visualized by collecting the fluorescence of rhodamine dye molecules dispersed in a polymer film on top of the Ag through the same objective.

In the infrared, surface plasmons propagating along a Ag/SiO_2 interface, excited with 1.49 μm light, are coupled to optically active erbium ions implanted in the SiO_2 at close proximity to the Ag interface. The propagation of these surface plasmons is studied in the far-field by two-dimensional imaging of the Er photoluminescence intensity at 1.53 μm using a confocal microscope. The surface plasmon modes are found to remain confined to stripe waveguides, and exponential decay of the mode intensity is observed with characteristic propagation lengths of $\sim$75 μm. The modes are excited at the Ag/SiO_2 interface of a Ag film by illumination from the air side of the film using two types of microstructures. First, gratings in 65 nm thick Ag films with a pitch of 3.3 μm allow first-order coupling to the mode at the air side at the same incident angle as second-order coupling to the mode at the SiO_2 side. This results in the possibility of surface plasmon cross-coupling, that enhances the excitation efficiency of surface plasmons at the SiO_2 side. Second, subwavelength hole arrays in optically thick films, optimized for excitation of the mode propagating at the Ag/SiO_2 interface, are used to launch surface plasmons into waveguides.

This imaging technique is a useful tool to investigate the propagation of bound surface plasmons (including long-range modes) in waveguides and optical components. Although numerous techniques exist to image (leaky) surface plasmons propagating at a metal/air interface, direct observation of bound modes in both symmetric and asymmetric dielectric environments is less straightforward.

Contents

1 Introduction **1**
- 1.1 Surface plasmon dispersion relation . . . 1
- 1.2 Coupling between surface plasmons and far-field radiation . . . 2
- 1.3 The damping of surface plasmons . . . 3
- 1.4 Imaging surface plasmons . . . 4
- 1.5 Outline of this thesis . . . 4

2 Surface plasmon modes in three-layer geometries **5**
- 2.1 Introduction . . . 5
- 2.2 Derivation of the dispersion relation . . . 5
- 2.3 Modes in an asymmetric environment . . . 7
- 2.4 Modes in a symmetric environment . . . 9
- 2.5 The influence of the bounding dielectrics on the long-range mode . . . 9
- 2.6 Long-range modes excited by oscillating dipoles . . . 11
- 2.7 Conclusions . . . 11

3 Coupling to surface plasmons at periodically corrugated surfaces **13**
- 3.1 Introduction . . . 13
- 3.2 Rigorous calculation of lamellar grating diffraction . . . 13
- 3.3 Coupling to surface plasmons through a metal film . . . 15
  - 3.3.1 Second order diffraction and cross-coupling . . . 15
- 3.4 Subwavelength hole arrays . . . 16

4 Microstructuring silver films **18**
- 4.1 Introduction . . . 18
- 4.2 Properties of silver films . . . 18
  - 4.2.1 Deposition and grain size . . . 18
  - 4.2.2 Optical properties and propagation lengths . . . 19
- 4.3 Fabrication steps . . . 20
  - 4.3.1 Electron-beam lithography . . . 20
  - 4.3.2 Grooves and gratings . . . 21
  - 4.3.3 Lift-off and adhesive layers . . . 21
- 4.4 Conclusions . . . 23

5 Imaging surface plasmons in the visible using fluorescent dye molecules **24**
- 5.1 Introduction . . . 24
- 5.2 Experimental . . . 24
- 5.3 Results and discussion . . . 25
  - 5.3.1 Propagation length . . . 25
  - 5.3.2 Excitation by microgratings and grooves . . . 26
- 5.4 Conclusions . . . 28

6 Excitation of erbium ions by surface plasmons **29**
6.1 Introduction . . . 29
6.2 Experimental . . . 29
6.3 Results . . . 30
6.4 Conclusions . . . 31

7 Imaging surface plasmons with erbium **32**
7.1 Introduction . . . 32
7.2 Experimental . . . 33
7.3 Results and discussion . . . 34
7.3.1 Surface plasmons on a cross-coupling grating . . . 34
7.3.2 Propagation lengths on a grating and on a smooth film . . . 36
7.3.3 Excitation of surface plasmons by hole arrays . . . 37
7.3.4 Propagation of the a_b mode on a metal stripe . . . 38
7.4 Conclusions and outlook . . . 39

Bibliography **41**

Acknowledgements **45**

Chapter 1

Introduction

Guiding light through optical fibers is one of the cornerstones of modern telecommunications. Long-range data transport at the standard wavelength of 1.55 μm is facilitated by erbium-doped fiber amplifiers, because of the intra-$4f$ transition in Er^{3+} ions that corresponds to a wavelength of 1.53 μm [1]. For future integrated optical devices that could combine optical signals with electronics in chip-size dimensions, it is important to be able to control the guiding and manipulation of light at very small scales. However, the down-scaling of optical waveguides runs into difficulties because the confinement of light is restricted to the diffraction limit. One possible route to achieving the desired spatial confinement of optical signals is to employ the use of surface plasmons on metallic structures.

Surface plasmons (SPs) are coherent oscillations of free electrons at an interface between a conductor and a dielectric, leading to electromagnetic fields confined to the interface [2, 3]. Because of the strong coupling between these excitations and electromagnetic radiation, the more accurate term of such an entity is a surface plasmon polariton, but the word 'polariton' will be omitted in the remainder of this thesis. These surface waves have transverse magnetic (TM) polarization, and are evanescent in both the dielectric and the metal, i.e. the field amplitude decays exponentially with distance from the interface.

In this work, the local excitation and propagation of surface plasmons is studied in the visible and in the infrared by detecting the photoluminescence of optical emitters placed at close proximity to the metal/dielectric interface along which surface plasmons are propagating [4]. We present a novel method to spatially map the propagation of surface plasmons at 1.5 μm propagating along a silver/glass interface, using Er ions as probes of the surface plasmon field intensity.

1.1 Surface plasmon dispersion relation

The special optical response of metals is apparent in their dielectric function $\epsilon(\omega)$ which generally has a large negative real part over a broad range of optical frequencies. We will define the field of a surface plasmon propagating along the x direction at the interface between a dielectric d and a metal m as [2]

$$\begin{aligned} E_d(x,z,t) &= E_{0d}e^{i(k_x x + k_{zd} z - \omega t)} && (z>0) \\ E_m(x,z,t) &= E_{0m}e^{i(k_x x - k_{zm} z - \omega t)} && (z<0). \end{aligned} \tag{1.1}$$

Maxwell's equations can be solved with the boundary conditions at the interface for any optical frequency ω, using appropriate dielectric functions $\epsilon_d(\omega)$ and $\epsilon_m(\omega) = \epsilon'_m(\omega) + i\epsilon''_m(\omega)$ for both materials [2]. For $\epsilon_m < 0$, $|\epsilon'_m| > \epsilon_d$, a solution is obtained that corresponds to an

evanescent surface plasmon mode, for which k_z has a large imaginary part in both media,

$$\begin{aligned} k_{zd} &= \frac{\omega}{c}\frac{\epsilon_d}{\sqrt{\epsilon_d+\epsilon_m}} \qquad (z>0) \\ k_{zm} &= \frac{\omega}{c}\frac{\epsilon_m}{\sqrt{\epsilon_d+\epsilon_m}} \qquad (z<0) \end{aligned} \tag{1.2}$$

and where the complex wave vector is given by

$$k_x = k_x' + ik_x'' = \frac{\omega}{c}\sqrt{\frac{\epsilon_d\epsilon_m}{\epsilon_d+\epsilon_m}}. \tag{1.3}$$

This equation gives the dispersion relation of surface plasmon modes propagating at a single metal/dielectric interface. The SP dispersion relation in more complex structures will be dealt with in chapter 2.

1.2 Coupling between surface plasmons and far-field radiation

The real part of the SP wave vector is plotted in Fig. 1.1 for a silver/air and a silver/glass interface, using the optical constants of Ag tabulated by Palik [5] and those of SiO_2 given in ref. [6]. A surface plasmon resonance occurs for the frequency where $\epsilon_m' = -\epsilon_d$. For all frequencies below this resonance, k_x is seen to be larger than the wave vector of light in the dielectric, $\sqrt{\epsilon_d}k_0$, approaching this value for small frequencies. This means that light incident from the dielectric cannot directly couple to surface plasmons and vice versa. Some mechanism must be introduced to effectively increase the wave vector of the incident light in order to achieve momentum matching. In this thesis, we focus on three methods to excite surface plasmons with an incident light beam, and to transfer part of their energy back into detectable far-field radiation:

- In Kretschmann-Raether coupling [2], a thin metal film is bounded between the dielectric d (e.g. air) and a prism with a higher refractive index ($\sqrt{\epsilon_p}$). For a certain incident angle θ_0, p-polarized light (i.e. **E** in the plane of incidence) that is totally reflected inside the prism can evanescently couple to SPs located at the opposing interface, if the coupling condition is satisfied:

  $$k_x = \sqrt{\epsilon_p}\frac{\omega}{c}\sin\theta_0 \tag{1.4}$$

  This effect is manifested as the attenuated total reflection (ATR) minimum of specular intensity at the resonance angle, and is strongest for a metal film thickness around 50 nm.

- Momentum can be added to the light wave by scattering at a surface corrugation. Although scattering at a single indentation or protrusion will allow part of the scattered radiation to couple to surface plasmons [7], the process is most efficient for diffraction at periodically spaced corrugations, that allow grating coupling to surface plasmons for a certain period a and incident angle θ_0:

  $$k_x = \sqrt{\epsilon_d}\frac{\omega}{c}\sin\theta_0 + ng = \sqrt{\epsilon_d}\frac{\omega}{c}\sin\theta_0 + \frac{2\pi n}{a}, \qquad n = \pm1, \pm2, \ldots \tag{1.5}$$

- Because the near-field of a dipole oscillating at a frequency ω contains wave vectors larger than $\sqrt{\epsilon}\omega/c$, optical emitters placed close to a metal/dielectric interface can couple to surface plasmon fields. We use the excitation of such emitters by surface plasmons in this thesis to probe the SP field intensity, by collecting the radiation that these molecules or ions emit into the far-field.

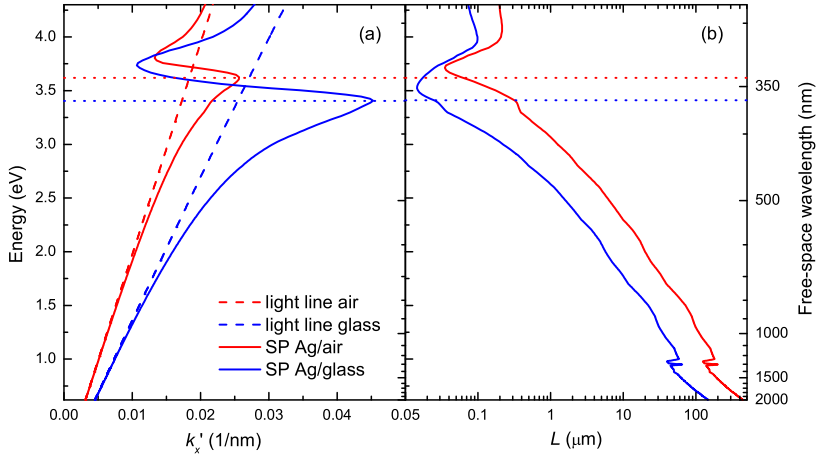

Figure 1.1: (a) Surface plasmon dispersion curves for Ag/air and Ag/glass interfaces. The surface plasmon modes exist below the surface plasmon resonance energies indicated by the dotted lines. (b) Propagation lengths for the surface plasmons in (a). The glass is fused silica and the optical constants of the silver are given by Palik [5].

1.3 The damping of surface plasmons

From equation 1.3 it is clear that surface plasmon waves experience significant damping k_x'' along x due to absorption in the metal. This is the main limiting factor to the practical use of surface plasmons for guiding optical signals, especially for frequencies close to the SP resonance. We can define the propagation length L as the $1/e$ decay length of the field intensity along x, or

$$L = \frac{1}{2k_x''} \approx \frac{c}{\omega}\left(\frac{\epsilon_d + \epsilon_m'}{\epsilon_d \epsilon_m'}\right)^{3/2} \frac{(\epsilon_m')^2}{\epsilon_m''} \tag{1.6}$$

The propagation length of SPs at a Ag/air and a Ag/silica interface is plotted as a function of photon energy in Fig. 1.1(b). Propagation lengths up to ~ 100 μm can be reached for infrared wavelengths, but near the surface plasmon resonance the damping increases very strongly. Besides ohmic damping, reradiation can significantly limit the SP propagation length. For example, surface plasmons at the air/metal interface of a thin film on glass will lose energy to leakage radiation into the glass; this is the converse process of Kretschmann-Raether coupling. Likewise, SPs on gratings can be strongly damped due to reradiation into a diffraction order, and all surface plasmons suffer from damping due to scattering at surface roughness.

We will see in chapter 2 that the SP damping will generally increase with decreasing metal film thickness. However, the surface plasmons at both interfaces of a thin metal film

in a symmetric dielectric environment can couple to form a mode that exhibits vanishing damping when the film thickness goes to zero [8]. These long-range surface plasmons (LR-SPs) are promising candidates for guiding electromagnetic signals on planar surfaces. The propagation of LR-SPs along thin metal stripes of a few μm width has been demonstrated experimentally [9, 10], yielding millimeter propagation lengths. An end-fire coupling technique can be used to excite these modes by aligning the output of an optical fiber to the end of a stripe waveguide [11], because their mode field distribution is very similar to that of modes in an optical fiber. Recently, various optical components in stripe waveguides have been developed to manipulate the flow of these LR-SPs [12, 13].

1.4 Imaging surface plasmons

In recent years, much effort has been undertaken to visualize surface plasmons propagating along structured metal films and stripe waveguides. The most important techniques used are photon scanning tunnelling microscopy [14–17], detecting far-field scattering of SPs at surface roughness [18], leakage radiation microscopy [19–21] and fluorescence imaging [4, 22]. We apply the latter to image infrared surface plasmons propagating at the Ag/glass interface of a Ag film on a glass substrate. This technique provides a useful tool to study the propagation and routing of LR-SPs and their interaction with photonic structures and optical components.

1.5 Outline of this thesis

In chapter 2, the surface plasmon modes that can propagate in dielectric/metal/dielectric structures are derived. The damping of these modes is seen to be strongly dependent on film thickness and the optical constants of the bounding dielectrics, and a certain range of geometries can sustain LR-SPs. Chapter 3 discusses the excitation of the different SP modes with gratings and subwavelength hole arrays, and demonstrates the use of a modal method to calculate lamellar grating diffraction and to estimate SP propagation lengths and coupling angles on gratings. Next, the fabrication of the structured silver films used in the experiments is described. Chapter 5 shows the use of the fluorescence imaging technique to study SPs excited with 532 nm light on grooves and gratings. The following chapter demonstrates the use of luminescent Er ions to probe surface plasmon field enhancements. In the last chapter, we report the local excitation of SPs with 1.49 μm light by gratings and hole arrays, and we study their propagation and damping by imaging grating reradiation and Er photoluminescence.

Chapter 2

Surface plasmon modes in three-layer geometries

2.1 Introduction

Most applications and experiments involving surface plasmons require the use of metal films of finite thickness. We mentioned that for Kretschmann-Raether coupling the thickness of the film is a crucial parameter. If the thickness is reduced, both the real and imaginary parts of the wave vector of a surface plasmon located at either one of the interfaces are altered by the presence of the other interface. Several reviews have been published about the possible coupled surface plasmon modes in such multilayer structures [11, 23, 24]. To calculate the dispersion and damping of the surface plasmon modes propagating along a smooth film, it is necessary to solve Maxwell's equations together with the boundary conditions at both interfaces. We will see that for thin films the propagation distance of most modes is drastically reduced, but a certain range of structures can also sustain long-range surface plasmons (LR-SPs). The difference between the permittivities of both bounding materials plays a large role in this case.

2.2 Derivation of the dispersion relation

Several optical modes can propagate along a thin metal film embedded in a dielectric environment. Their dispersion and damping are characterized by the complex propagation constant $k_x = k_x' + ik_x''$. We are interested in transverse-magnetic (TM) modes propagating in the positive x direction, in a system consisting of a thin metal slab with thickness h and dielectric constant $\epsilon_2 = \epsilon' + i\epsilon''$. The metal film is bounded by dielectric media 1 and 3, and we will take $\epsilon_1 \leq \epsilon_3$ as a convention. From the wave equation we can, in accordance with Raether's derivation of the surface plasmon dispersion relation at a single interface [2], assume the **H** field in medium i to be of the form

$$\begin{aligned} H_{i,x}(x,z,t) &= 0 \\ H_{i,y}(x,z,t) &= H_0 f_i(z) e^{i(k_x x - \omega t)} \\ H_{i,z}(x,z,t) &= 0. \end{aligned} \tag{2.1}$$

The z dependency in the three media is given by

$$f_1(z) = e^{-ik_{z1}z} \quad (z<0) \tag{2.2}$$
$$f_2(z) = c_1 e^{ik_{z2}z} + c_2 e^{-ik_{z2}z} \quad (z<0<h) \tag{2.3}$$
$$f_3(z) = c_3 e^{ik_{z3}z} \quad (z>h), \tag{2.4}$$

where we note that in this sign convention, a wave that is purely evanescent in dielectric i will correspond to a negative imaginary k_{zi}. With the Ampère-Maxwell law, the components of the electric field can be determined:

$$E_{i,x}(x,z,t) = \frac{i}{k_0\epsilon_i}\frac{\partial}{\partial z}H_{i,y}(x,z,t) \tag{2.5}$$
$$E_{i,y}(x,z,t) = 0 \tag{2.6}$$
$$E_{i,z}(x,z,t) = -\frac{k_x}{k_0\epsilon_i}H_{i,y}(x,z,t) \tag{2.7}$$

By applying the boundary conditions for all fields at both interfaces, the explicit forms of the functions $f_i(z)$ are obtained,

$$f_1(z) = e^{-ik_{z1}z} \tag{2.8}$$
$$f_2(z) = \cosh(ik_{z2}z) + \frac{\epsilon_2 k_{z1}}{\epsilon_1 k_{z2}}\sinh(ik_{z2}z) \tag{2.9}$$
$$f_3(z) = f_2(h)e^{ik_{z3}(z-h)}, \tag{2.10}$$

together with the dispersion relation for the three-layer geometry [11]:

$$\tanh(ik_{z2}h)(\epsilon_1\epsilon_3 k_{z2}^2 + \epsilon_2^2 k_{z1}k_{z3}) - \epsilon_2 k_{z2}(\epsilon_1 k_{z3} + \epsilon_3 k_{z1}) = 0 \tag{2.11}$$

We can now try to solve this dispersion equation for k_x by using the relations

$$k_{z1}^2 = \epsilon_1 k_0^2 - k_x^2 \tag{2.12}$$
$$k_{z2}^2 = \epsilon_2 k_0^2 - k_x^2 \tag{2.13}$$
$$k_{z3}^2 = \epsilon_3 k_0^2 - k_x^2, \tag{2.14}$$

which follow from the wave equation. Modes with different characteristics will be obtained. If for example a solution is found for $k_{z3} = \sqrt{\epsilon_3 k_0^2 - k_x^2}$, the corresponding field in medium 3 will be radiative (propagating away from the film) for $k_x' < \sqrt{\epsilon_3}k_0$. The field amplitude will grow exponentially with increasing z because the mode is damped in the x direction (it will of course not grow when we examine it along the direction of energy flow in medium 3). Considering that, the fact that the field amplitude goes to infinity for large z is in itself not enough reason to discard a damped mode as unphysical. Such a mode is called *leaky* (l) into dielectric 3 [25]. A solution is said to be *bound* (b) if the field amplitude decays with increased distance from the film.

The modes can also be differentiated by their field (and corresponding charge) distribution across the film. An *antisymmetric* (a) mode corresponds to an antisymmetric charge distribution, a symmetric distribution of E_x and an antisymmetric distribution of E_z and H_y. It can in general be recognized by the fact that the latter fields exhibit a zero inside the film. A *symmetric* (s) mode has charges of equal sign on the opposing interfaces, an antisymmetric distribution of E_x and a symmetric distribution of E_z and H_y [11]. In an asymmetric dielectric environment, of course no field distribution is truly symmetric or antisymmetric, but in the thick film limit the antisymmetric modes can still be recognized by a node inside the film [26]. Note that in references [2, 27], the symmetric/antisymmetric terminology is reversed.

Equation 2.11 is solved numerically using a Nelder-Mead minimization algorithm. The values of k_x thus obtained have at least 6-digit precision. We will first consider the case

of a silver film between a fused silica substrate and air, before solving for the modes in a symmetric dielectric environment. In all cases, the optical constants of the silver are obtained by interpolation of the Palik data set [5], and the index of refraction of the fused silica glass ($\epsilon \approx 2.1$) is given by a polynomial approximation [6].

2.3 Modes in an asymmetric environment

In the general case of a metal slab between different dielectric media, such as air and glass, four modes can always be found. They correspond to different solutions to equations 2.12 and 2.14. Their field distributions are displayed in Fig. 2.1, and their dispersion and damping as a function of film thickness are shown in Fig. 2.2 for energies corresponding to free-space wavelengths of 532 nm and 1490 nm. The two antisymmetric modes a_l and a_b become degenerate when the thickness h is large, in which case they correspond to a surface plasmon at a single Ag/glass interface. The a_b mode is bound in all media, but the a_l mode is leaky into the low-index dielectric ϵ_1. The symmetric modes s_l and s_b have the highest field concentrations at the Ag/air interface. They have a smaller wave vector than the antisymmetric modes and correspond to a surface plasmon at the Ag/air interface for infinite film thickness.

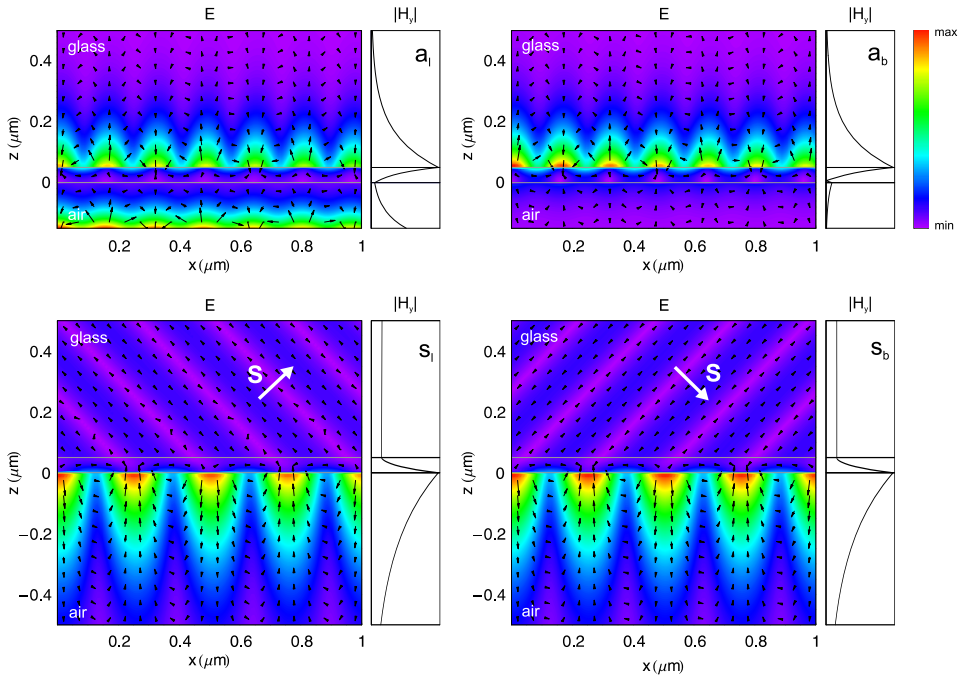

Figure 2.1: Field distributions of the four modes with a free-space wavelength of 532 nm, sustained by a 50 nm silver film on a fused silica substrate. Displayed are colored contour plots of the magnitude of the real part of **E**, vector plots of the **E** field and graphs of the amplitude of **H** at $x = 0$. The white arrows indicate the direction of energy flow given by the complex Poynting vector **S**.

The solutions a_b and s_l have been observed in many experiments, and their interpretation is straightforward. The a_b mode is evanescent in both the glass and the air regions, whereas the s_l mode is leaky into the glass because k_x lies to the left of the light line in that dielectric in the dispersion diagram (Fig. 1.1). The field in medium 3 can be put in the form of an angular spectrum of plane waves with frequency ω by viewing the metal/glass interface as a sheet consisting of an infinite number of line sources of the radiation field, with a relative

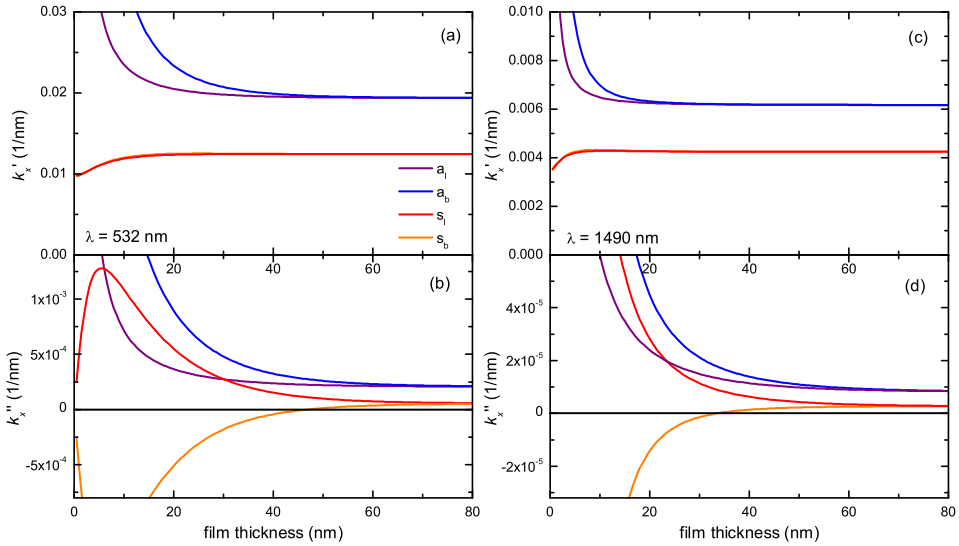

Figure 2.2: Dispersion and damping for $\lambda = 532$ nm, (a) and (b), and for $\lambda = 1490$ nm, (c) and (d), as a function of film thickness for the modes in a Ag film surrounded by fused silica and air.

phase and strength determined by k_x' and k_x''. The diffraction integral then predicts the angular power dependency of the leakage radiation into the glass [28, 29]

$$f(\theta) \propto \frac{\cos^2\theta}{(k_x' - \sqrt{\epsilon_3}k_0 \sin\theta)^2 + (k_x'')^2} \tag{2.15}$$

where θ is the angle relative to the surface normal. This spectrum is sharply peaked for the s_l mode, with a peak width proportional to the damping k_x''. The other leaky mode (a_l) does not exhibit such a peak, since k_x' is in that case larger than the wave vector of light in both media. Instead, this mode radiates into the low-index dielectric in a broad range of angles. The angular dependencies of both leaky modes are compared in Fig. 2.3. Because the antisymmetric mode lies to the right of the light line, the contribution of leakage radiation to the total loss of this mode is much smaller than for the symmetric mode.

The symmetric bound (s_b) mode shows decreased damping for reduced film thickness. The propagation length in fact reaches infinity at a certain cutoff thickness h_c, which can be calculated by solving Eq. 2.11 for k_x' and h, while taking $k_x'' = 0$ in Eqs. 2.12-2.14. Below h_c, $k_x'' < 0$ and the mode corresponds to a growing wave. At the cutoff thickness, this solution to Maxwell's equations can be easily interpreted as an instance of the ATR resonance, when we look at the field distribution (Fig. 2.1). For this specific value of h, an incident field from the high index dielectric is totally absorbed by the film by coupling to a surface wave. But also for thicknesses above h_c, the long-ranging s_b mode must be supported by a wave incident from the high permittivity side.

Burke et al. [11] provide a further discussion on the excitability of the modes a_l and s_b, by assessing their influence on the field of a line source parallel to the y direction positioned in the neighborhood of a metal film. Such a line source can for instance consist of a continuous row of dipoles placed along y, all pointing in the x direction. They show that both solutions offer no contribution to the reflected power of the line source for this particular geometry. Since any source can be seen as a superposition of line sources, the a_l and s_b modes cannot

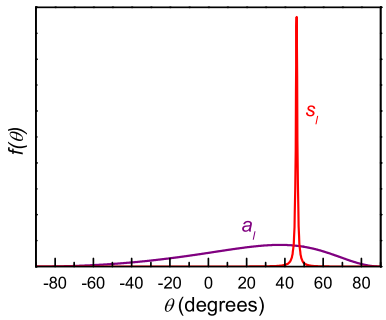

Figure 2.3: Angular spectrum of power radiated by leaky modes s_l and a_l in an air/Ag/glass environment for $\lambda = 532$ nm. The power spectrum of the a_l mode is multiplied by a factor 1000.

be excited and sustained for a finite propagation distance by the metal film. They only have physical significance when coupled to incoming or outgoing radiation fields, as was pointed out for the s_b mode above. By illumination of a metal film with thickness h_c at the ATR resonance angle through a prism, coupling to a surface plasmon will occur, that can propagate outside the region of excitation as a s_l mode. This method of local Kretschmann-Raether coupling is widely used for the excitation of (leaky) surface plasmon modes into stripe waveguides [30, 31].

2.4 Modes in a symmetric environment

When the metal slab is surrounded by similar dielectrics, it is necessary that the fields are truly symmetric or antisymmetric with respect to the center of the film. In this case only two solutions can exist, the well-known bound modes s_b and a_b [8, 32]. For a silver slab of 20 nm surrounded by fused silica glass, the field distributions of the waves with an energy corresponding to a free-space wavelength of 1490 nm are shown in Fig. 2.4, and the dispersion with film thickness in Fig. 2.5. The symmetric, high energy mode is generally termed the long-range surface plasmon (LR-SP), and exhibits millimeter scale propagation lengths. It is therefore widely applicable for waveguiding purposes [9, 10], but only at the cost of a relatively low confinement to the film [27]. The antisymmetric, low energy mode is confined to the metal much stronger, but it has a very large damping. In a practical situation, the dielectric constants of both surrounding media will not be exactly the same. It is therefore interesting to study the behavior and existence of the LR-SP mode for small differences between the permittivities ϵ_1 and ϵ_3.

2.5 The influence of the bounding dielectrics on the long-range mode

We have seen that in the asymmetric environment a long-range mode exists above a certain cutoff thickness h_c. If the difference between the dielectric constants of the bounding media becomes smaller, this s_b mode transforms to the long-range mode in the symmetric environment. The inset of Fig. 2.6 shows the cutoff thickness as a function of the ratio ϵ_1/ϵ_3. As mentioned above, the solution for the asymmetric case generally needs a plane wave incident on the film from the high-index side, and is therefore not a real mode, in the

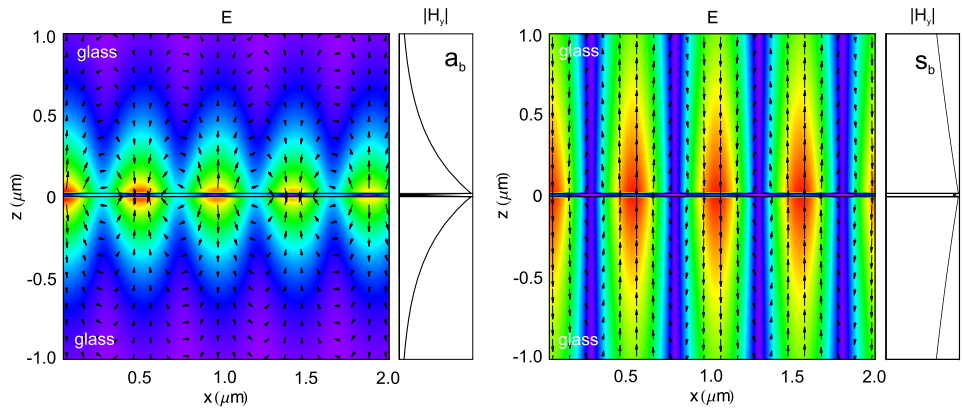

Figure 2.4: Field distributions of the two modes with a free-space wavelength of 1490 nm, sustained by a 20 nm silver film embedded in fused silica. Displayed are colored contour plots of the magnitude of the real part of **E**, vector plots of the **E** field and graphs of the amplitude of **H** at $x = 0$.

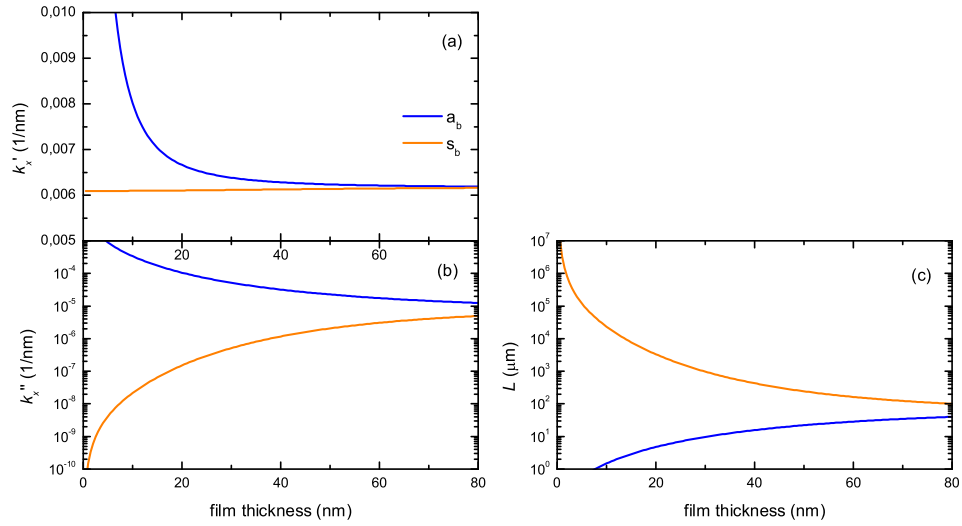

Figure 2.5: Dispersion (a), damping (b) and propagation distance L (c) for $\lambda = 1490$ nm, as a function of film thickness for the modes in a Ag film symmetrically surrounded by fused silica.

sense that it is useful for waveguiding. If however the difference between the dielectric media is small enough, the wave vector of the symmetric mode can lie to the right of *both* light lines ($k_x > \sqrt{\epsilon_3}k_0$), and the solution no longer requires an incident plane wave. But for a particular difference between ϵ_1 and ϵ_3, this only happens for some thickness $h > h_c$. At this point, also the symmetric leaky mode switches character to a mode that is leaky into a broad range of angles. Similar to the a_l mode before, this is not an observable solution. The nature of the transition from the s_l mode to the long-ranging s_b mode as the dispersion curve crosses the high-index light line has to my knowledge not been studied experimentally. For a more detailed theoretical discussion, see refs. [11, 24, 33].

Figure 2.6 shows the propagation length of the s_b mode for different values of ϵ_1/ϵ_3. We

see that for a relative difference in the dielectric constants of 1%, millimeter propagation lengths are possible. But due to the existence of a cutoff thickness, the damping will depend strongly on the metal film thickness and on the optical constants of all materials. Another point of interest is that the long-range modes in metal stripe waveguides of finite width, as calculated by Berini [34], contain several maxima along the y direction for $\epsilon_1 \neq \epsilon_3$. Hence, they may be more difficult to excite, either by end-fire coupling or by coupling to surface plasmons on an extended thin film.

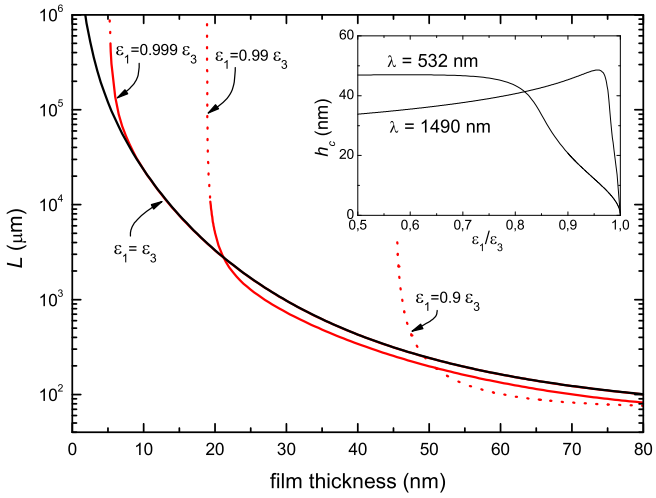

Figure 2.6: The propagation length of the s_b mode for slightly asymmetric structures as a function of film thickness. The dashed lines correspond to solutions with $k_x' < \sqrt{\epsilon_3}k_0$. The free-space wavelength is 1490 nm. Inset: The cutoff thickness as a function of ϵ_1/ϵ_3.

2.6 Long-range modes excited by oscillating dipoles

As mentioned in section 2.3, surface plasmon modes can be excited by harmonic oscillator dipoles placed in the direct vicinity of the metal film. The power dissipated by such a dipole can be determined for all in-plane wave vectors $k_{||}$ using a model developed by Ford and Weber [35, 36], that calculates the reflected field at the position of the dipole from the Fresnel reflection and transmission coefficients. Figure 2.7(a) shows the power dissipation spectrum of Er^{3+} ions that have an emission wavelength of 1.53 μm, when placed at 50 nm from a 20 nm thick silver film ($\epsilon = -84 + 8.5i$ from [5]) embedded in fused silica. For $k_{||}/\sqrt{\epsilon}k_0 < 1$, it shows the decay due to spontaneous emission. For $k_{||}/\sqrt{\epsilon}k_0 > 1$ two resonances are visible, that correspond to the excitation of the s_b mode (small k_x, small damping) and the a_b mode (large k_x, large damping). Power dissipation spectra for structures with slightly different values of ϵ_1 are displayed in more detail around the s_b resonance ($k_x \approx \sqrt{\epsilon_3}k_0$) in Fig. 2.7(b). The transition from the leaky to the bound symmetric mode, that occurs when k_x crosses the light line in medium 3, occurs in this case just below $\epsilon_1 = 0.99\epsilon_3$.

2.7 Conclusions

In dielectric/metal/dielectric structures, four solutions to Maxwell's equations can be found that correspond to surface plasmon waves confined to the metal film. However, at any one

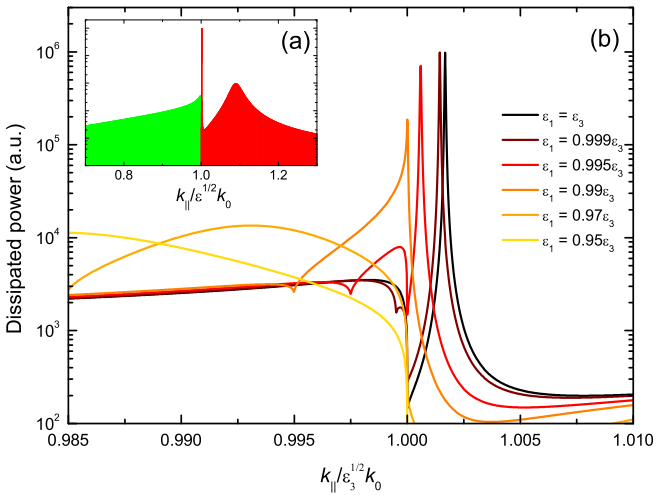

Figure 2.7: (a) Power dissipation spectrum of Er^{3+} ions placed at 50 nm from a 20 nm silver film embedded in fused silica. The spectrum shows decay into spontaneous emission (green) and surface plasmons (red). (b) Same as (a), for varying differences between the bounding media 1 and 3. Peaks correspond to excitation of a symmetric surface plasmon mode.

particular energy and set of optical constants, only two of those solutions are modes that are useful for waveguiding purposes. The modes can be either bound in all media, or leaky into the high-index medium. If the permittivities of the bounding dielectrics are brought closer together, the symmetric solution can cross the high-index light line and change character from a leaky mode to a bound mode with potentially a very large propagation length. The damping and existence of this mode depends strongly on small variations in thickness and optical constants.

Chapter 3

Coupling to surface plasmons at periodically corrugated surfaces

3.1 Introduction

As we have seen in the first chapter, one way to achieve momentum matching between light and surface plasmons is to introduce periodic corrugations in a metal surface. An incident plane wave can be diffracted by such a grating into diffraction orders, a few of which correspond to propagating plane waves. The other orders are of evanescent nature, and these can resonantly drive surface charge oscillations to form a surface plasmon when the incident light is p-polarized and Eq. 1.5 is satisfied [37]. Both k'_x and k''_x can be significantly altered for SPs on gratings with respect to their values on smooth films.

The **E** field of the evanescent-diffracted order is 90° out of phase with the incident light, and because this field drives the surface plasmon at resonance an extra 90° phase shift is introduced in the surface plasmon field. The surface plasmons can reradiate to light emerging at the same angle as the specularly reflected (zeroth order) beam through the same mechanism, so this reradiation is in phase with the incident beam. However, the specularly reflected light is in antiphase with the incident light, so it interferes destructively with the SP reradiation resulting in a reflectivity minimum for the resonance incident angle θ_0 [38]. In analogy with the ATR minimum, the zeroth order reflectance R_0 around this resonance can be approximated classically by a Lorentz profile [37]. If R_0 is plotted as a function of $k_{\|} = (\omega/c)\sin\theta + ng$ instead of θ, the position of the minimum gives the value of k'_x for the surface plasmon on the grating, while the full width at half maximum (FWHM) is approximately equal to $2k''_x$. The maximum efficiency of coupling to surface plasmons is obtained from the depth of the resonance.

These parameters have been studied both theoretically and experimentally for different grating geometries and frequencies [2, 39–42], reporting efficiencies close to 100% for certain grating profiles. Here we will discuss some of the issues concerning the periodic structures that are used in the experiments described in chapters 5 and 7. We will use an adapted modal method [43] to estimate the complex SP wave vectors on gratings.

3.2 Rigorous calculation of lamellar grating diffraction

As mentioned above, to learn more about the excitation and damping of surface plasmons on gratings it is instructive to know the reflection and transmission efficiencies into all diffraction orders of different kinds of grating structures, when a plane wave is incident under an angle θ with respect to the surface normal. The rigorous calculation of the fields

under such conditions has been performed using a variety of approaches for many types of grating profiles [37].

Because of the anisotropic nature of the fabrication techniques (see chapter 4), the shape of the grating grooves produced in this work is approximately rectangular. The optical response of such lamellar gratings is notoriously difficult to model with many formalisms because of the discontinuity of the dielectric function along the x axis. The numerical method employed here to overcome this difficulty is a generalization of the method of 'exact eigenvalues and eigenfunctions' [44], that is described in reference [43]. In this modal approach [37], the lamellar grating structure is viewed as a stack of layers containing rectangular rods with different optical constants. The fields inside each rod are expanded in a suitable basis of eigenfunctions [44]. Using a number of eigenfunctions large enough to reach convergence, the corresponding eigenvalues are found by applying the boundary conditions between the layers of rods. Matching the modal expansions with the Rayleigh-expanded fields outside the grating yields the fraction of energy in all far-field diffracted orders.

All theoretical propagation lengths of SPs on gratings that are mentioned in chapters 5 and 7 were calculated with this method. As an example, R_0 is plotted in Fig. 3.1(a) against the first-order diffracted $k_{\|}$ for 633 nm light incident on gratings of 1 μm pitch in a 100 nm Ag film. The sharp feature for an incident angle just below the surface plasmon resonance, indicated by the arrow, is caused by the redistribution of energy among the diffraction orders as the $n = 1$ diffraction order disappears below the horizon, i.e. its angle with the surface normal is 90°. We note here that the first order diffraction into angles just below 90° is typically 10 times smaller for s polarization than for p polarization. Figure 3.1(b) shows the wave number and damping of the surface plasmon mode on the gratings, obtained from the resonance positions and halfwidths in (a). As expected, both the real and imaginary parts of the SP wave vector show approximately quadratic dependence on groove depth [41]. For this particular geometry and 633 nm incident light, we see that the propagation length is equal to the grating pitch for a groove depth of 80 nm.

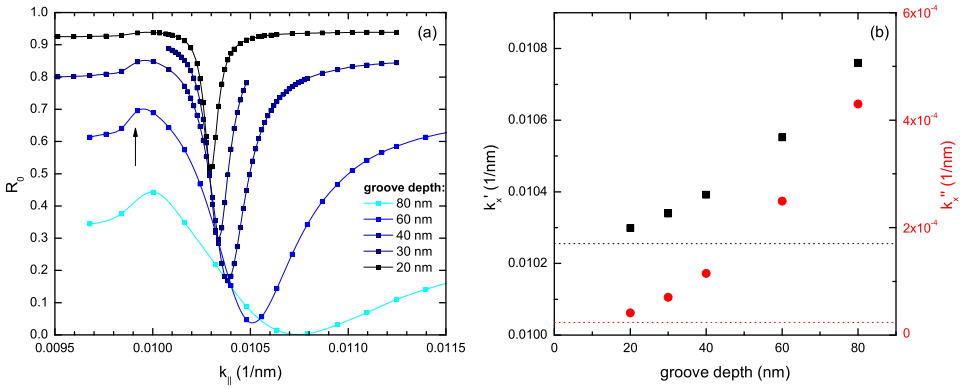

Figure 3.1: (a) Calculated reflection into zeroth diffraction order R_0 as a function of $k_{\|}$ for 633 nm light incident on conformal lamellar gratings of 1 μm pitch in a 100 μm Ag film on glass (optical constants from [5]). Below the value of $k_{\|}$ marked by the arrow, the +1 diffracted order is a propagating plane wave. (b) Real and imaginary part of the SP wave vector obtained from the reflection spectra in (a). The dotted lines correspond to the values for a smooth Ag film.

3.3 Coupling to surface plasmons through a metal film

We are interested in the excitation of surface plasmons at the metal/glass side of a metal film on a glass substrate by illumination from the air side. Conformal grating shapes, i.e. geometries in which the profiles of the air/metal and metal/glass interfaces are identical and in phase with each other, are of particular importance because they are generally formed when evaporating a metal on a corrugated surface. Schröter and Heitmann [45] reported that the grating coupling of light incident from the glass side of a film at normal incidence to SPs propagating at the air side of the film is not possible for a conformal grating geometry. Hooper and Sambles [38] provided an insightful theoretical argument to explain why this coupling is so weak, that can be extended to first-order coupling to SPs at the glass side of the film for non-normal incidence from the air side of the film. They point to the fact that two routes are possible for first order coupling to a SP at the opposite side of a film: either the +1 order diffracted at the first interface can couple evanescently to the SP at the other interface, or the beam transmitted through the film can be +1 diffracted at the second interface (Fig. 3.2(a)). Both involve first order diffraction and attenuation through the film, so their efficiency is comparable, but Hooper and Sambles showed that they interfere destructively, resulting in only very weak SP excitation.

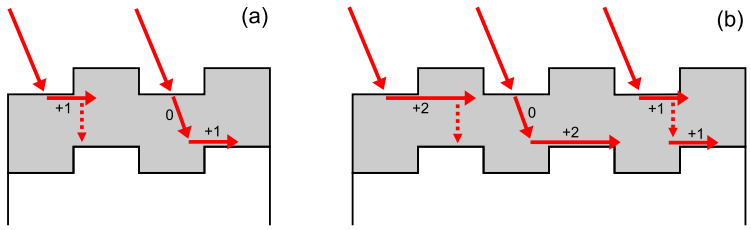

Figure 3.2: Schematic of most important coupling schemes that contribute to the coupling of light incident from the air side of the film to a SP propagating at the substrate side of the film. (a) First-order (+1) coupling, (b) second-order (+2) coupling.

3.3.1 Second order diffraction and cross-coupling

The same argument does not necessarily hold for second order coupling, since in that case a third excitation path is possible (Fig. 3.2(b)): the +1 diffracted order produced at the first interface (which will be evanescently decaying across the film) can be +1 diffracted again at the second interface to achieve momentum matching to the SP at that interface. Figure 3.3(b) shows R_0 and the fraction of incident power dissipated in the film (A) around the resonances that correspond to the excitation of SPs at a Ag/glass interface with +1 and -2 order diffraction (at 32.5° and 23°, respectively). The structure is a conformal grating in a 45 nm Ag film with a pitch of 1.6 μm and a groove depth of 30 nm, illuminated by 1.49 μm light from the air side. The resonance caused by +1 coupling is indeed small, and the fact that the shape of the resonance in R_0 is not a regular minimum is an indication of interference of different contributions. Although the -2 resonance is somewhat larger, its efficiency is still only 1%, because destructive interference can play a role here as well and because second order diffraction is generally less efficient than the first order process.

It might be possible to enhance this second-order coupling by increasing the efficiency of the third coupling scheme in Fig. 3.2(b). The magnitude of the first-order evanescent-diffracted field at the metal/air interface reaches a maximum when it can excite a surface plasmon at that interface [38]. Thus it is believed that maximum second-order coupling to SPs at the metal/glass interface can be achieved when under the same conditions first-order coupling to SPs at the metal/air interface is possible. This condition is satisfied for a

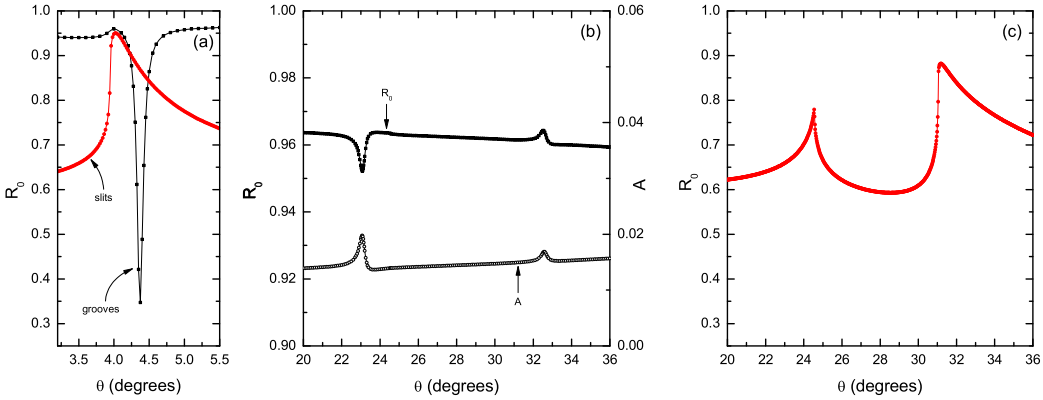

Figure 3.3: Comparison of the reflection of periodic structures in a 45 nm Ag film (optical constants displayed in Fig. 4.2) on fused silica with a pitch of 1.6 μm, illuminated by 1.49 μm light incident at an angle θ from the air side of the film. (a) R_0 around the resonance caused by +1 coupling to SPs at the metal/air interface for a conformal grating with 30 nm deep grooves and an array of 400 nm wide slits. (b) R_0 and total absorption A by the conformal grating with 30 nm grooves showing the -2 and +1 resonances of coupling to SPs at the metal/glass interface. (c) R_0 for an array of 400 nm wide slits in the same angular region as (b), showing strong effects caused by +1 and -2 diffraction orders.

particular grating pitch a and can be written as

$$k_{x,glass} - k_{x,air} = \frac{2\pi}{a} \tag{3.1}$$

The surface plasmons at opposite sides of such a grating are said to be cross-coupled. The enhanced transmission of optical energy through a metal film by the cross-coupling effect described above has been demonstrated by exciting optical emitters placed close to a grating in a metal film, and collecting their fluorescence at the other side of the film [46–49]. Large enhancements of the transmitted fluorescence were found for wavelengths for which 3.1 was satisfied. Enhanced transmission through this mechanism would also be expected to be evident from diffraction calculations. In Fig. 3.4 the reflection into the zeroth diffraction order R_0 is plotted for different grating pitches around the value that allows cross-coupling to occur, together with the total transmitted fraction of the energy T and the total absorption $A = 1 - R - T$. The gratings have a conformal geometry with grooves of 46 nm depth in a 65 nm Ag film, illuminated by 1.49 μm light. For the grating with 3.28 μm pitch, two separate resonances can be distinguished that correspond to the two SP modes. The excitation of the Ag/air mode is roughly 20 times more efficient than the excitation of the Ag/glass mode. When they overlap, indeed a small enhancement in the total transmission is seen, although it is not as large as expected based on the reported peaks in photoluminescence transmission [47, 48]. Further investigation and a more detailed comparison of all diffraction orders is needed to obtain the relation between structural parameters and cross-coupling efficiency.

3.4 Subwavelength hole arrays

When a grating does not have a conformal profile, i.e. when a periodic thickness modulation is introduced, it is no longer impossible to excite SPs at the opposite side of the film through

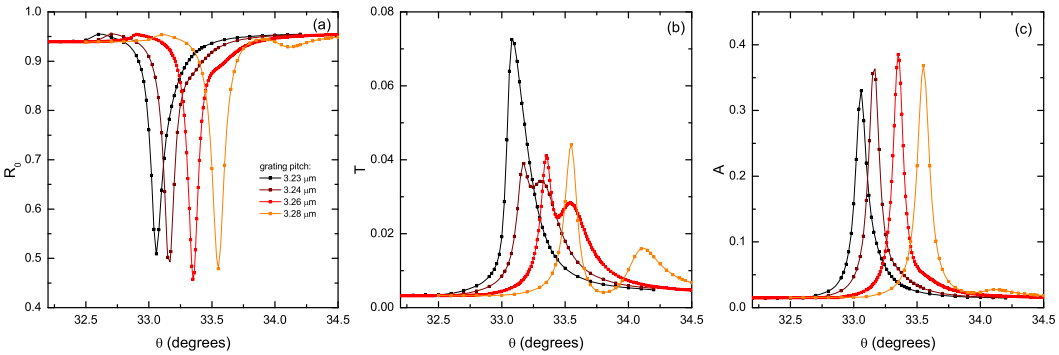

Figure 3.4: Reflection into zeroth order R_0, total transmission T and absorption A for 1.49 μm illumination of 46 nm deep conformal gratings in a 65 nm Ag film (optical constants displayed in Fig. 4.2) on fused silica, for pitches that allow different degrees of SP cross-coupling.

first-order coupling. One such structure that could be easily fabricated is an array of slits. Figure 3.3 (c) shows R_0 for an array of 400 nm wide slits in a 45 nm thick Ag film with a periodicity of 1.6 μm, illuminated with 1.49 μm light. It shows strong effects due to first- and second-order diffraction, but no clear resonances that correspond to +1 or -2 coupling to SPs at the Ag/glass interface. As the comparison with a 1.6 μm pitch conformal grating shows in Fig. 3.3(a), there is also no evidence for first-order grating coupling to a SP at the air side of the film. Although a single slit can excite surface plasmons [50], an array of slits seems to be incapable of supporting them, unless one considers very narrow slits [51].

A related structure that *is* known to excite surface plasmons on both interfaces is a periodic array of subwavelength holes. The transmission spectra of light through two-dimensional hole arrays in optically thick metal films show distinct peaks [52], that have generally been related to the excitation of surface plasmons at both interfaces of the film [52–57]. Although the dispersion and damping of surface plasmons are strongly changed on the hole array with respect to their values on a smooth film, the coupling condition for a rectangular distribution of apertures is roughly given by [53]

$$\vec{k}_{SP} = \vec{k}_0 \sin\theta_0 + i\vec{g}_x + j\vec{g}_y, \qquad i,j = \pm 1, \pm 2, \ldots, \tag{3.2}$$

where $\vec{k}_{SP}$ is the surface plasmon wave vector, $\vec{k}_0$ the incident wave vector and $\vec{g}_x$ and $\vec{g}_y$ the grating vectors corresponding to the spatial periods a_x and a_y along both axes of the array. The peaks in the transmission spectrum can then be attributed to the excitation of SPs for different (i, j).

In chapter 7, hole arrays of finite lateral dimensions are used to launch surface plasmons propagating on a smooth Ag film. This principle has been demonstrated before in refs. [58–60]. Just like for excitation of a surface plasmon 'beam' by a regular micrograting, the intensity of the beam emerging from a hole array will depend on the coupling efficiency, the propagation length on the grating and the wave vector difference between SPs on the array and on the smooth film. All factors are strongly influenced by the shape and size of the grating profile or the holes [54, 61–63], by the refractive indices of the bounding dielectrics, and by the frequency of the light.

Chapter 4

Microstructuring silver films

4.1 Introduction

The field of plasmonics has taken a big leap in recent years, but only after the development of techniques to fabricate the micro- and nanostructures needed to control the flow and storage of electromagnetic energy on a very small scale. We have seen that the periodic corrugation of metal surfaces provides an important way to couple light to planar surface plasmons and vice versa. To obtain large-scale gratings in metal films for these purposes, holographic photolithography techniques have been widely used [39–41]. However, local excitation and control of surface plasmons asks for other structuring techniques, of which electron-beam lithography (EBL) and focused ion beam (FIB) irradiation have proven to be the most important because of their ability to define diverse structures with high resolution. We apply the former, in combination with reactive ion etching (RIE) and lift-off techniques, to fabricate micrograting and hole arrays in Ag films. In this chapter the fabrication steps of these processes are described, but we will first discuss the properties of the deposited silver films.

4.2 Properties of silver films

4.2.1 Deposition and grain size

The deposition of Ag films on glasses raises some important issues, due to the low binding energy of Ag on glass. This generally results in large grain sizes, that determine the surface roughness and associated scattering of surface plasmons. High roughness causes increased damping [2], and the scattered radiation can even be used to image the propagation of surface plasmons [18].

The growth process of thin metal films can be characterized by three stages. First, aggregates of metal atoms nucleate by diffusion of the atoms on the substrate surface. Increasing the deposition rate causes a higher density of relatively smaller nuclei, and increasing the substrate temperature causes a lower density of larger nuclei [64]. Moreover, because the binding energy of Ag on SiO_2 is low, the nucleation rate will be small, and large nuclei will be formed. Next, the nucleation centers grow to form a closed film (from $\sim$15 nm upwards [65]) consisting of columnar grains. Finally, the grain boundaries in this unstable system can migrate to minimize the energy associated with the boundaries and with the grain surface [66]. Because [111] planes have minimal surface energies in a fcc crystal, grains with this orientation can grow much faster than others [67–69]. This process of secondary grain growth is dominated by diffusion across grain boundaries, and is thus highly dependent on temperature.

In the experiments described in this thesis, all metal films have been vacuum-deposited by thermal evaporation, except the hole array structures, for which electron beam deposition has been employed. In the case of thermal evaporation, the source material was evaporated through resistive heating, at a vacuum pressure smaller than $5 \cdot 10^7$ mbar. In electron beam evaporation, the material was heated by irradiation with an intense electron beam, at pressures below $1 \cdot 10^8$ mbar. Both deposition techniques are highly directionally anisotropic. Scanning Electron Microscopy (SEM) images of Ag films deposited on SiO_2 substrates by thermal evaporation at two different evaporation rates are shown in Figs. 4.1(a) (0.11 nm/s) and (b) (2.2 nm/s).

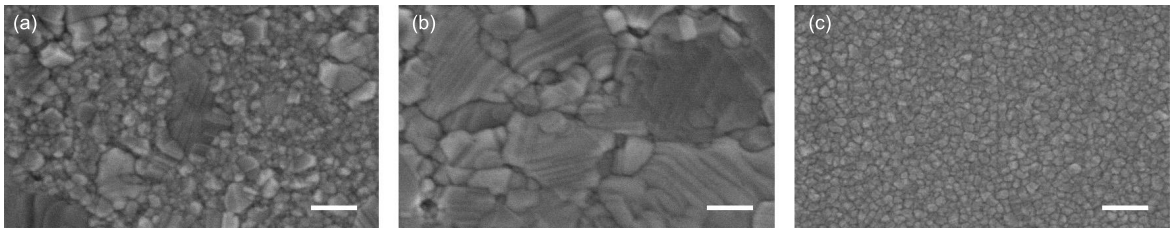

Figure 4.1: SEM images of (a) a 45 nm thick Ag film thermally evaporated at 0.11 nm/s on a thermally grown SiO_2 film on silicon, (b) a 50 nm thick Ag film thermally evaporated at 2.2 nm/s on thermal oxide, (c) a 200 nm thick Ag film sputtered at 0.08-0.4 nm/s on thermal oxide. Scale bars are 200 nm.

Comparing these images, it seems that a large evaporation rate results in larger grains, in contradiction with expectations. This may be explained by a higher substrate temperature of the Ag film for higher evaporation rates, since the temperature was not controlled during these depositions. The fact that the grain size distribution is obviously inhomogeneous is an indication of secondary grain growth, favoring the fast growth of [111] oriented grains. A higher temperature could significantly enhance this process, although it should be noted that in the case of thin films, this annealing even takes place at room temperature [68].

Although smaller grains are expected to lead to smaller scattering, it is not immediately clear that these large secondary grains would be detrimental to surface plasmon propagation, since the number of grain boundaries is reduced, and this can in principle lead to smaller roughness [66]. However, as will be seen further on, the grains of the Ag film determine the roughness of the side walls of grooves and holes in the film. Therefore, the evaporation rate when depositing Ag directly on glass was kept at 0.01-0.03 nm/s for the first 10 nm, and kept below 0.07 nm/s for the evaporation of the rest of the film, in order to obtain small grains.

An alternative to evaporation is sputter deposition. In this case Ag atoms are sputtered from a target by bombardment with argon ions. Figure 4.1(c) shows a 200 nm thick Ag layer, sputtered at a rate that rose from 0.08 to 0.4 nm/s during the deposition. The grain size seems to be much more homogeneous than for evaporation. Due to the isotropic character of sputtering, the smallest features that can be made by sputtering a film on a corrugated substrate are not as small as those made by evaporation. Moreover, its isotropic character causes sputtering to be incompatible with lift-off, because it will always result in a closed film (see section 4.3.3). But it could still be a useful technique, for example to deposit thin films on gratings, if the grating depth is required to be larger than the film thickness. In that case it would be desirable to improve the control of deposition rate and substrate temperature.

4.2.2 Optical properties and propagation lengths

Experimentally obtained optical constants of silver films have been tabulated by Palik [5] and Johnson and Christy [70], among others, but their values are found to differ significantly.

In Figure 4.2(a), the dielectric function $\epsilon = \epsilon' + i\epsilon''$ of a 65 ± 1 nm thick Ag film deposited by thermal evaporation on a fused silica substrate, as measured with ellipsometry, is compared to these literature values. The thickness of the Ag film was determined in multiple places

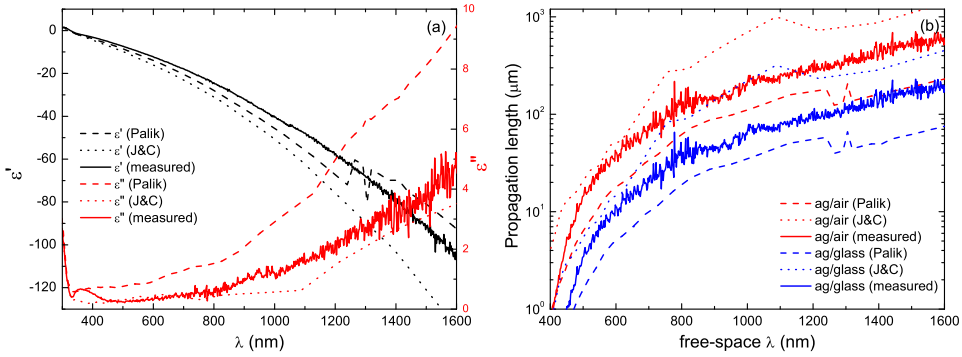

Figure 4.2: (a) Real (ϵ') and imaginary (ϵ'') parts of the dielectric function of Ag as given by Palik [5] and Johnson and Christy [70], and as measured with ellipsometry on a 65 nm thick Ag film on fused silica. (b) SP propagation lengths in absence of scattering, calculated from the optical constants shown in (a), for Ag/air and Ag/glass interfaces.

on the sample by measuring the depth of scratches in the film with a surface profiler. The measured value was in very good agreement with the thickness of the film obtained from fitting ellipsometric data. Reale [71] has found that both the optical constants and the density of a thin film differ significantly from bulk values below 30 nm thickness. That is why it is desirable to perform density-independent thickness measurements.

The low reproducibility of optical constants, even when deposition parameters are kept constant, makes it hard to predict SP propagation lengths. Figure 4.2(b) shows the propagation lengths on perfectly smooth Ag/air and Ag/glass interfaces calculated from the data given in Fig. 4.2(a).

4.3 Fabrication steps

The microstructures that are fabricated in Ag films for the experiments described in this thesis are gratings and hole arrays. The process steps used to create both types of structures are illustrated in Fig. 4.3.

4.3.1 Electron-beam lithography

With EBL, patterns can be defined in a resist layer by exposure of the resist to an electron beam. The electrons induce the breaking of chemical bonds in the resist material, which makes it more soluble in a developer solution.

Polymethylmethacrylate (PMMA) resist films were spin-coated on 500 μm thick fused silica substrates (Suprasil, Hereaus), and on thermal oxide on silicon. The substrates were cleaned just before spin-coating with a 5:1:1 H_2O:H_2O_2:NH_4OH solution. For the fabrication of gratings, 2 wt.% PMMA (950k) in chlorobenzene was spin-coated at 4500 rpm for 50 seconds, resulting in 100 nm thick films after 5-15 minutes baking on a hot plate at 175°C. For the fabrication of hole arrays, two-layer resist stacks were spin-coated to create an undercut effect after EBL, that is important for successful lift-off. First, a 3 wt.% 495k PMMA solution in chlorobenzene was spin-coated at 2400 rpm for 45 seconds and baked

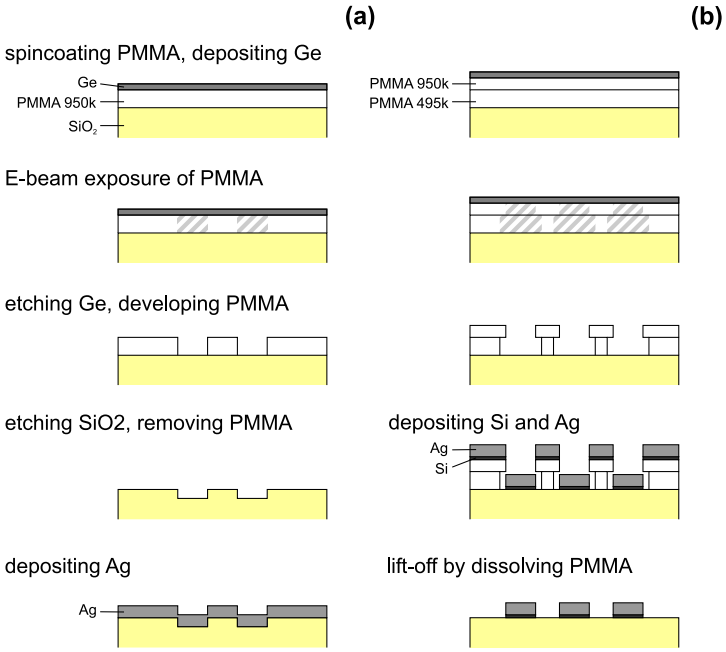

Figure 4.3: Schematic overview of the procedure to fabricate (a) gratings and grooves in Ag films, and (b) hole arrays in silver films of limited lateral dimensions.

at 175°C to obtain a 150 nm PMMA film. Second, a 2 wt.% 950k PMMA solution was spin-coated at 3000 rpm for 45 seconds and baked at 175°C, resulting in a top layer of 120 nm thickness. Ge layers of 15-18 nm thickness were evaporated on top of the PMMA layers to make the samples conductive.

The PMMA was exposed to a 30 kV electron beam using an electron-beam pattern generator (Jeol JSM 6460), at doses of 280-450 μC/cm^2. After removing the Ge layer with RIE using a SF_6/O_2 plasma, the PMMA was developed with a 1:3 mixture of methylisobutylketone and 2-propanol (a 1:2 mixture was used for the hole arrays to increase the undercut effect).

4.3.2 Grooves and gratings

Grooves and grating structures patterned in the PMMA were anisotropically etched into the SiO_2 substrate by RIE of the SiO_2 with a CHF_3/Ar plasma. The PMMA was subsequently removed with a O_2/Ar plasma. Metal films were evaporated onto the samples as described above. Figure 4.4 shows the resulting corrugations in 50 nm thick Ag film. Before evaporating Ag, a 5 nm Cr layer was deposited on the substrate to increase the Ag adhesion and reduce the grain size. To obtain uniform groove widths in a grating, the electron dose of the outmost grooves has to be higher than that of the central grooves, because the latter receive a higher effective dose due to electrons that are backscattered during the exposure of neighboring grooves ('proximity effect'). The side wall roughness of the grooves is of the order of 10 nm, and is mainly determined by the Ag grains.

4.3.3 Lift-off and adhesive layers

For the fabrication of hole arrays, the metal film was evaporated on the patterned PMMA, which was then dissolved in acetone at 60°C, leaving metal on the substrate only where the PMMA was removed. The problem of poor adhesion of Ag films on glass is especially

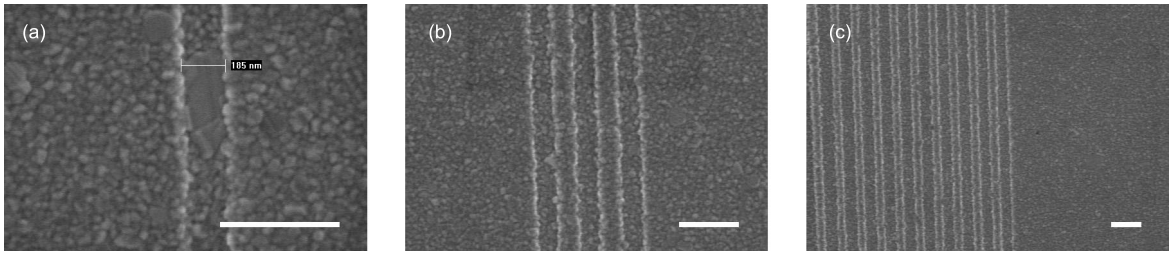

Figure 4.4: (a) SEM image of a 180 nm wide groove in a 50 nm thick Ag film on thermal oxide, with a 5 nm thick Cr adhesion layer. A 170 nm wide field was written in the PMMA at a dose of 456 μC/cm^2. The depth of the groove in SiO_2 was 46 nm before evaporation. (b) SEM image of 170 nm wide grooves spaced 360 nm apart on the same sample as (a). 170 nm wide fields were written at a dose of 432 μC/cm^2. (c) SEM image of part of a grating with 320 nm pitch on the same sample as (a). 160 nm wide fields were exposed with a dose of 360 μC/cm^2. The outmost grooves received up to 6% higher dose to compensate for proximity effects. Scale bars are 500 nm.

important for this lift-off technique. The standard solution to this problem is to evaporate a thin (2-5 nm) film of Cr or Ti before the deposition of Ag. However, these materials have a large extinction coefficient, which has a large influence on the damping of the a_b surface plasmon mode located at the Ag/glass interface. Dipole power dissipation calculations as described in section 2.6 show that a 2 nm layer of Cr or Ti causes k_x'' to be 3 or 2.7 times as large, respectively, as it would be without the adhesive layer (for a wavelength of 1490 nm, using optical constants given in [5]). Therefore, we use Si as an adhesive layer, which has no absorption in the infrared. A 4 nm thick Si film causes k_x'' to be only 1.2 times as large as in the absence of the film, due to an increase of the effective dielectric constant. Ag layers of 96 nm thickness on top of 4 nm thick Si films were deposited by electron beam evaporation at 0.01-0.05 nm/s.

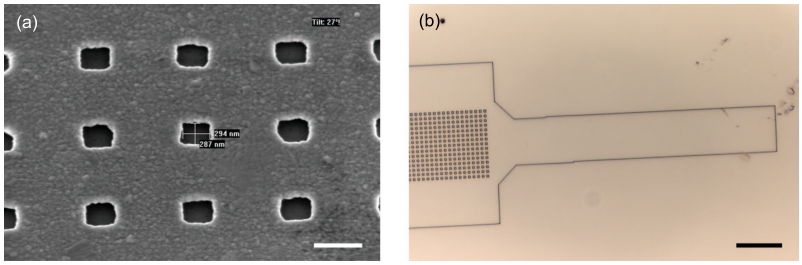

Figure 4.5: (a) SEM image of a hole array of 1.02 μm pitch in a 60 nm thick Ag film on a silicon substrate. The scale bar is 500 μm. (b) Bright field reflection microscopy image of a hole array structure of 2 μm pitch connected to a waveguide in a 95 nm Ag film on fused silica, before lift-off. The scale bar is 20 μm.

Hole arrays of 1-2 μm pitch and various hole sizes were fabricated in this manner in Ag areas of finite lateral dimensions on fused silica substrates. The hole arrays were connected to 20 μm wide, 115 μm long Ag stripe waveguides. A microscope image of such a structure before lift-off is displayed in Fig. 4.5(b). Figure 4.5(a) shows a SEM image of a detail of a hole array that was fabricated in the same way on a silicon substrate, after successful lift-off. On glass, the lift-off of the holes was not completely successful, as most of the Ag 'caps' remained attached to the film (Fig. 4.6(c)). After sonication in acetone for 4 seconds, a significant number of caps was removed (Fig. 4.6(a) and (b)), but this step also risks detaching other parts of the film from the substrate. The problem could most probably be solved by increasing the thickness of the bottom PMMA layer to at least three times the Ag thickness.

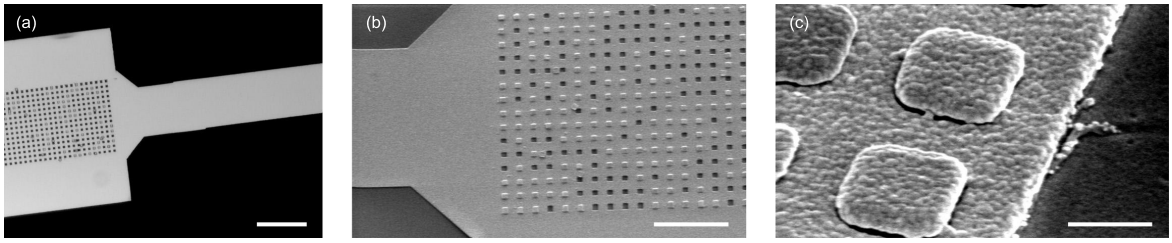

Figure 4.6: (a) Bright field reflection microscopy image of the structure shown in Fig. 4.5(b) after lift-off and sonication. The scale bar is 20 μm. (b) SEM image of a hole array of 2 μm pitch after lift-off and sonication. The defined hole diameter was 1 μm, and the electron dose was 325 μC/cm^2. The scale bar is 10 μm. (c) SEM image of a detail of a hole array after lift-off, showing that the caps on the holes are still attached to the film. The scale bar is 500 nm.

4.4 Conclusions

Surface roughness plays an important role in the damping of surface plasmons. The roughness is determined by growth conditions during the first stages of film deposition, and by the development of grain boundaries after deposition. It would be useful to study the dependence of surface plasmon damping on film deposition rate and temperature, for example by performing ATR measurements. It is expected that fast evaporation at low substrate temperatures will yield the best results, possibly in combination with annealing after deposition.

Hole arrays, gratings, grooves and stripe waveguides have been fabricated in Ag films using EBL. Usually, hole arrays are fabricated by FIB milling metal films after deposition. This technique is superior to EBL in combination with lift-off because of its high resolution, but EBL can be a fast alternative to fabricate large hole arrays designed to show extraordinary transmission of infrared wavelengths (see Fig. 7.5). Although here Si adhesive layers were used to facilitate lift-off on glass substrates, it has been reported that Ag waveguides can be made directly on SiO_2 by lift-off [13], and it would be valuable to be able to do the same.

Chapter 5

Imaging surface plasmons in the visible using fluorescent dye molecules

5.1 Introduction

One of the techniques for visualizing locally excited surface plasmons propagating along structured metal films is to place luminescent dyes close to the metal film, as reported in reference [4]. The dyes can be excited by the surface plasmon field and subsequently emit radiation into the far field, which is detected with a CCD camera through a microscope objective. In this way a spatial mapping of the SP field distribution is obtained. However, the fluorescence of dye molecules in direct contact with a metal surface will be completely quenched, and the excitation and emission rates will depend strongly on the distance to the metal surface. A polymer film of several tens of nanometers doped with dye molecules can be a useful way to achieve the required homogeneous distribution of distance to the metal film [22]. Here we present the use of this technique to image surface plasmons excited with 532 nm laser light incident on micrograting and grooves in an Ag film. The fluorescent dye used is rhodamine, which has a broad emission spectrum around 550 nm.

5.2 Experimental

Gratings of approximately 10×15 μm and grooves of 15 μm length were fabricated in a 780 nm thick thermal oxide film on a silicon substrate, as described in chapter 4. The pitch of the gratings was varied from 300 to 620 nm, and gratings with grooves in two perpendicular directions were made, to allow both *s*- and *p*-polarized excitation without rotating the sample or the polarization of the incident beam. The grating depth after etching of the SiO_2 was measured with a surface profiler to be 46 nm. A 50 nm Ag film was evaporated on the sample at a rate of 0.07 nm/s, after the deposition of a 5 nm Cr adhesion layer.

To obtain homogeneous fluorescent dye layers, rhodamine 575 (Exciton) powder was dissolved in a 2 wt.% solution of PMMA in chlorobenzene. Only a small fraction of the 0.17 g/l rhodamine actually dissolved after sonicating several times for 30 minutes at 30°C, but this was enough to change the color of the solution. The solution was then spin-coated on the sample at 6000 rpm, and the resulting PMMA layer was baked at 130°C for 15 minutes. The thickness of the layer was approximately 75 nm.

The sample was illuminated using polarized 532 nm emission from a frequency-doubled

Nd:YAG laser, focused through a 60× Nikon objective with a numerical aperture (NA) of 0.8. Spatially resolved fluorescence was projected through the same objective onto a color CCD camera, after passing through a 532 nm notch filter to block the reflected laser light (Fig. 5.1).

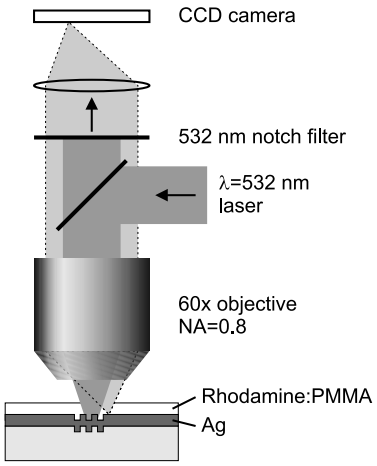

Figure 5.1: Schematic of the setup used.

5.3 Results and discussion

The 532 nm laser light was focused onto grating structures of varying pitch. For all gratings under *p*-polarized illumination (electric field perpendicular to the grating grooves), the fluorescence intensity on the grating (Fig. 5.2(c)) was enhanced as compared to the fluorescence collected when the excitation beam was focused on an unstructured part of the silver film (Fig. 5.2(a)). For grating pitches between 300 and 420 nm, the shape of the fluorescence spot was clearly stretched in the direction perpendicular to the grating grooves. Moreover, when the laser was focused on the edge of the grating, i.e. on the outer groove, a fluorescence stripe was protruding from the grating edge (Fig. 5.2(b)). None of these effects were visible for *s*-polarized excitation (Figs. 5.2(d-f)).

5.3.1 Propagation length

One indication for the fact that the stripe observed in Fig. 5.2(b) is indeed due to a surface plasmon excited at the outer groove or grooves of the micrograting is the clear polarization dependency. Another indication is the observed exponential decay. In Figure 5.3 the fluorescence intensity is plotted as a function of the distance from the grating edge. The excitation spot was just inside a grating of 320 nm pitch. The fitted line corresponds to a propagation length of 2.0 μm.

The dispersion and damping of surface plasmons in this geometry are significantly altered by the 75 nm PMMA layer, which has a refractive index of 1.49. Calculations of the decay of a dipole in the PMMA layer into surface plasmon wave vectors, as described in section 2.6, estimate the surface plasmon wavelength in these structures to be 355 nm for a dipole frequency corresponding to 532 nm. The expected propagation length, determined from the width of the calculated resonance, would be approximately 1.6 μm, but this value depends strongly on errors in the optical constants and thicknesses of all layers. It is however in reasonably good agreement with the observed propagation length of 2 μm.

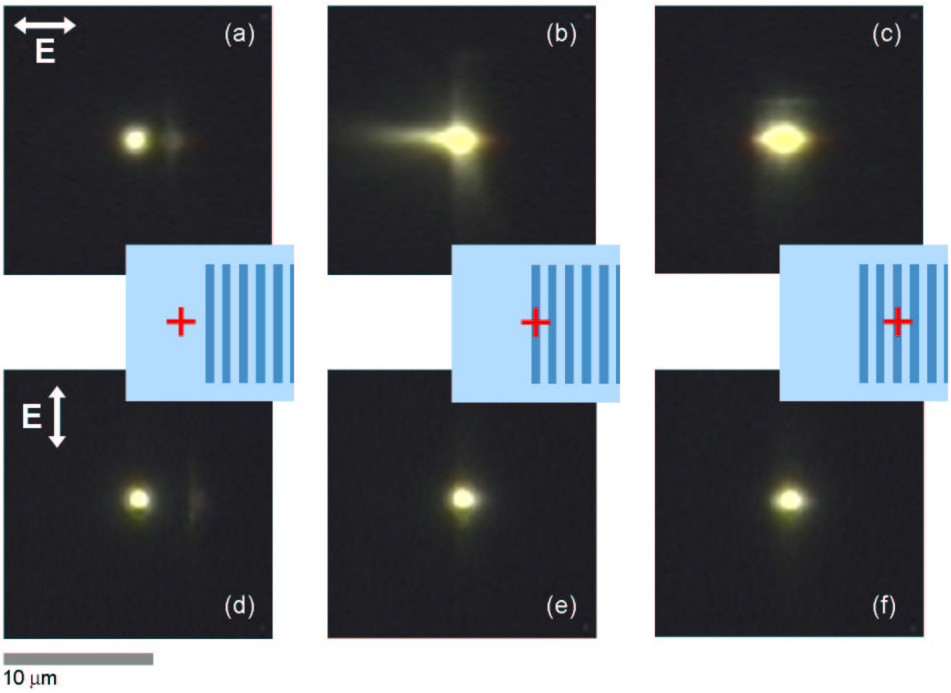

Figure 5.2: Micrographs of rhodamine fluorescence for *p*-polarized (a-c) and *s*-polarized (d-f) excitation. The laser was focused just outside a micrograting (a,d), on the edge of the grating (b,e) and in the middle of the grating (c,f). The grating pitch is 360 nm and the excitation wavelength is 532 nm.

5.3.2 Excitation by micrograting and grooves

Because a high NA objective is used, the radiation incident on the gratings is distributed in a broad range of angles. Therefore only a small part of the incident radiation can couple to surface plasmons via grating coupling for any particular grating pitch, and a broad range of pitches will allow the coupling condition (Eq. 1.5) to be satisfied. Since the laser beam inside the microscope has a gaussian profile, the distribution of excitation angles will have a maximum around 0 degrees. Maximum coupling would therefore be expected on gratings with a pitch comparable to the surface plasmon wavelength. This may be an explanation for the fact that for grating pitches larger than 420 nm, the observed fluorescence spot was less stretched in the direction of polarization.

The absence of the SP stripes when the excitation beam is focused on the middle of the grating can be mainly attributed to increased damping on the grating. With the reflection spectra calculations described in chapter 3 we can estimate the propagation length on the grating with a pitch of 360 nm to be less than 500 nm. This distance is too short to be able to resolve surface plasmon stripes on the grating, propagating outside the region of excitation. That is why SP stripes are only observed in the direction out of the grating, when excited on the outermost grooves of the grating.

The excitation of surface plasmons by single and multiple ridges in an Ag film has been investigated experimentally in reference [7]. Figure 5.4(a) shows a fluorescence image of SP stripes propagating in both directions, excited on a single groove with the same depth as the gratings and 180 nm width. When three grooves spaced 360 nm apart are illuminated, SPs launched in both directions are observed as well, but in this case their relative intensity depends on the position of the excitation spot. If the laser light is focused to the right of the center of the three grooves, as shown in Fig. 5.4(b), the SP propagating to the left is

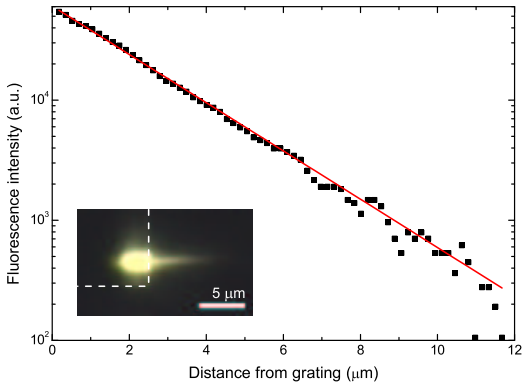

Figure 5.3: Fluorescence intensity (squares) along a surface plasmon stripe with distance from a grating with 320 nm pitch. The fitted line has a decay length of 2.0 μm. The inset shows the complete fluorescence image, where the edge of the grating is indicated by the dashed line.

poorly transmitted by the grooves. This is again an indication of the strong scattering of the SP by the grooves. Sánchez-Gil and Maradudin [72] have calculated the back reflection and radiative scattering of surface plasmons by ridges and grooves of gaussian shape. They have found that for groove widths smaller than the wavelength, typically more than half of the SP energy is scattered into radiation by a single groove.

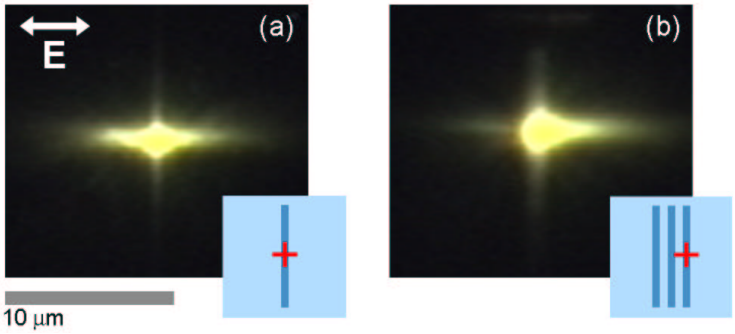

Figure 5.4: (a) Fluorescence microscopy image of SP stripes excited by *p*-polarized 532 nm light incident on a groove of 46 nm depth and 180 nm width. (b) Same, for 532 nm light focused slightly off the center of three grooves of 170 nm width, which are spaced 360 nm apart.

A critical note should be added, because these experiments provide no definitive proof that the observed stripes can indeed be attributed to surface plasmon fields. We have mentioned in chapter 3 that, like surface plasmon coupling, grazing angle grating diffraction is also more efficient for *p*-polarized light. Because of the broad range of excitation angles, light will also be diffracted into a broad range of angles. The resulting increase in pump power provides one explanation for the fluorescence enhancement of the rhodamine dye above a grating. A second explanation is that surface plasmons generated by the decay of the dye in the vicinity of the Ag film can be coupled out to detectable radiation by the grating [73, 74]. In this case, the observed dependence on pump polarization could arise from the significant steady-state polarization anisotropy of rhodamine fluorescence [75]. Thirdly, surface plasmons could of course be generated by illumination of the grating, which would cause

a field enhancement in the dye layer close to the metal film. As for the observed fluorescence stripes, however, we believe that the confirmation of their exponential decay with calculations, together with the strong polarization dependency, provides enough evidence to attribute their existence to surface plasmons.

5.4 Conclusions

Surface plasmons were excited by the 532 nm illumination of grooves in Ag films, and visualized by imaging the 550 nm fluorescence of rhodamine in a PMMA layer. This technique provides a relatively quick and simple way to study the propagation of SPs [4].

The presence of the polymer layer significantly reduces the SP propagation length to 2 μm, in accordance with calculations. On gratings, the damping is increased even more due to reradiation losses, so SP stripes cannot be discerned with the resolution of a regular bright field microscope. Even if the excitation spot would be larger, enlarging a grating beyond a few periods would not cause a more intense surface plasmon beam to emerge from the grating in this case. Choosing the grating dimensions more carefully, more efficient coupling might be reached. Outside the grating, the propagation length would be most significantly improved by reducing the thickness of the polymer layer, e.g. by using a different spin-coating technique. The damping could also be decreased by using a thicker Ag film, thereby reducing the leakage radiation losses into the substrate, and by decreasing the thickness of the Cr adhesion layer, which has considerable absorption.

One of the main disadvantages of the fluorescence imaging technique is the photobleaching of the dye. This phenomenon poses severe limits to reproducible and quantitative analysis of the propagation of surface plasmons on structured films using fluorescent dye molecules.

Chapter 6

Excitation of erbium ions by surface plasmons

6.1 Introduction

One of the main features associated with surface plasmons is the high confinement of the field to the direct vicinity of a metal/dielectric interface. This property has driven a lot of research employing surface plasmons, for example in sensing applications and in guiding electromagnetic waves below the diffraction limit. The high field confinement potentially allows efficient excitation of luminescent probes embedded in the dielectric close to a metal film. In this chapter we study the angle-dependent excitation of erbium ions by surface plasmons generated using Kretschmann-Raether coupling. Glass prisms are widely used to excite surface plasmons at a metal/air interface. With a prism of higher refractive index, coupling to surface plasmons at a metal/glass interface is allowed by illumination under the proper angle from the high index side of the metal film. Er ions implanted just below the surface of a glass substrate have been shown to be able to couple to surface plasmons at a metal/glass interface [36, 76]. Here we show that they can act as a probe of the SP-induced field enhancement at the metal/glass interface.

6.2 Experimental

A fused silica substrate (suprasil, Heraeus) was doped with Er by 150 keV Er^+ ion implantation with a fluence of $7 \cdot 10^{15}$ Er/cm^2, resulting in a peak Er concentration of 3 at.%. The sample was then annealed in vacuum for one hour at 900°C to remove any implantation damage [1]. The estimated range and straggle of the Er ions is 60 and 13 nm, respectively, as calculated with the Monte Carlo program TRIM [77]. Half of the sample was covered with an Ag film by thermal evaporation at a rate of 0.01-0.05 nm/s. The thickness of the film was determined to be 48 ± 1 nm with a surface profiler. An equilateral SF11 glass prism (with an index of refraction $n = 1.80$ at 515 nm) was clamped to the sample, with a Cargille index matching fluid (index of refraction 1.63) filling the space between the prism and the evaporated side of the sample.

Laser light of 515 nm from an Ar-ion laser was focused through the prism onto the sample by a 6.3× objective under a variable angle. This laser emission is resonant with higher level absorption transitions in Er^{3+} [1]. The incident light was p-polarized, i.e. the electric field was in the plane of incidence. The 1530 nm photoluminescence (PL) of the Er ions was collected through the back side of the substrate by a $f = 10$ cm lens and passed through a monochromator onto a liquid-nitrogen cooled Ge diode. The laser light was modulated by

an acousto-optical modulator and the PL intensity and decay traces were measured using a standard lock-in technique.

6.3 Results

Figure 6.1 shows Er PL decay curves with and without presence of the Ag film. At $t = 0$ the pump intensity was switched off. It is clear that in both cases the decay is not single exponential. After ~ 2 ms, both curves are approximately single-exponential, with decay rate $W \approx 160\ \mathrm{s}^{-1}$ without the Ag film, and $W \approx 300\ \mathrm{s}^{-1}$ with the Ag film. The faster decay of Er in the vicinity of an Ag/glass interface has been reported elsewhere [36], and is mainly attributed to the decay of Er into surface plasmons for this implantation depth. There are two possible explanations for the fact that the decay is not single exponential. On the one hand, the variation of the Er concentration across the gaussian implantation profile can lead to a variation in the decay rate due to concentration quenching [1]. This phenomenon involves the Förster transfer of energy between Er ions to quenching sites [78]. However, the observable variation in decay rates that can be attributed to this effect is usually very small. On the other hand, the appearance of a fast component in the PL decay can be attributed to a process called cooperative upconversion, in which one excited Er ion is promoted to a higher energy state at the cost of the excitation of another Er ion [79]. Further investigation is required to confirm this hypothesis.

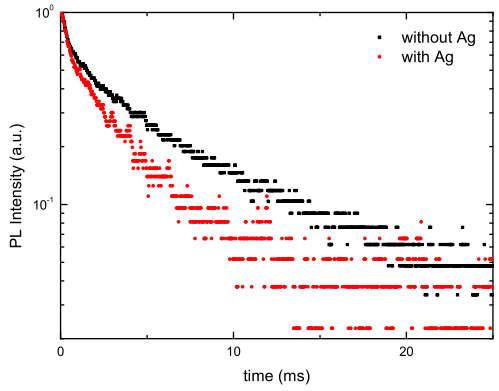

Figure 6.1: Decay traces of the PL intensity of Er ions implanted in fused silica glass at a depth of 60 nm, near a fluid/glass and a Ag/glass interface.

The electromagnetic fields in the multilayer structures investigated induced by the 515 nm laser illumination from the SF11 prism side can be calculated with a standard transfer matrix method [80]. This evaluates the angle-dependent Fresnel reflection and transmission coefficients r and t from the complex refractive indices and thicknesses of all the layers in the structures: the SF11 prism, the $n = 1.63$ fluid, the Ag film and the fused silica substrate. The refractive index of Ag is taken to be $0.047+2.8i$ (see section 4.2.2), and that of the fused silica glass is 1.46. The magnitude of the electric field at the surface of the glass ($|E_{glass}|$) is derived from [2]

$$\frac{|E_{glass}|^2}{|E_{0,prism}|^2} = \frac{\epsilon_{prism}}{\epsilon_{glass}} \frac{|H_{glass}|^2}{|H_{0,prism}|^2} = \frac{\epsilon_{prism}}{\epsilon_{glass}} |t|^2, \tag{6.1}$$

where $E_{0,prism}$ is the electric field of the incident plane wave in the SF11 prism. It is of course more relevant to compare the electric field at the glass surface with the electric field

of the incident light inside a hypothetical glass prism. We will thus define the field intensity enhancement as

$$\frac{|E_{glass}|^2}{|E_{0,glass}|^2} = |t|^2. \tag{6.2}$$

Figure 6.2 shows the measured Er PL intensity at 1530 nm for various angles of the pump beam inside the prism, with and without the Ag film. The oscillatory behavior of the PL intensity as a function of angle in the structure without the Ag film is due to interference of the pump beam in the fluid layer. By fitting the calculated field intensity enhancement (the red curve in Fig. 6.2(a)) to the oscillatory pattern in the PL intensity data, the thickness of the fluid layer is determined to be 1.0 μm. The height of the intensity enhancement curve was matched to the experimental data. As can be seen in Fig. 6.2(a), even in the case without the Ag film the intensity at the fluid/glass interface is significantly enhanced. This can be readily understood because for incident angles just below the Brewster angle, the angle of a beam transmitted into the low-index glass is close to 90 degrees, and the cross-sectional area of that beam is very small. For angles just above the Brewster angle, the incident wave is totally internally reflected, and an evanescent surface wave is excited [81].

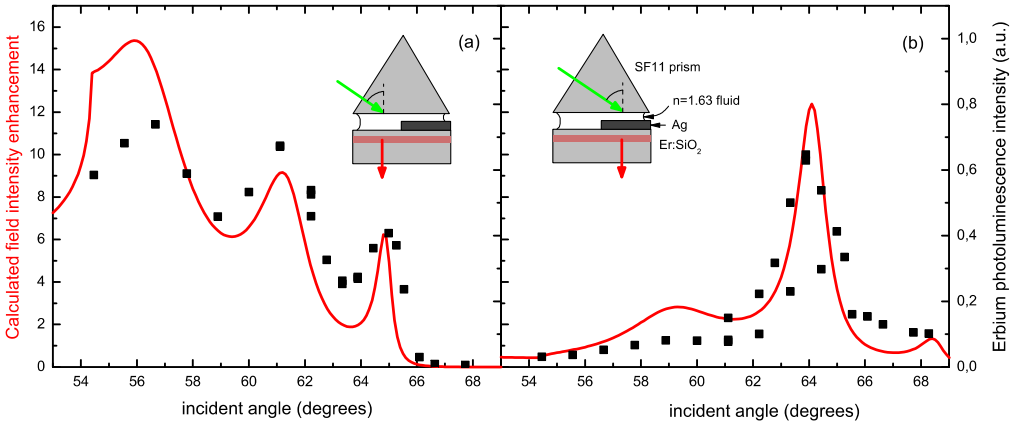

Figure 6.2: PL intensity (squares) for various excitation beam angles inside the prism, with (b) and without (a) the presence of a 48 nm Ag film. The red curves are the calculated field intensity enhancements for both configurations, where the $n = 1.63$ fluid layer has an assumed thickness of 1.0 μm.

Keeping the fitted fluid thickness and scaling factor constant, we can calculate the expected field intensity enhancement including the 48 nm Ag layer. Comparison with the experimental PL intensity shows reasonably good agreement (Fig. 6.2(b)). A clear surface plasmon resonance is observed around an incident angle of 64 degrees.

6.4 Conclusions

Er ions implanted in glass have been shown to act as a probe of the field enhancement at a Ag/glass interface due to surface plasmons excited by prism coupling. The observed PL intensity as a function of pump angle is in good agreement with calculations, which predict a twelvefold field intensity enhancement for the geometry under study. However, if an index matching fluid with the same refractive index as the prism would be applied between the prism and the Ag film, calculations predict an enhancement of more than 80 times. This would allow efficient excitation of Er, and could therefore be useful for studying high pump power dependent effects like cooperative upconversion.

Chapter 7

Imaging surface plasmons with erbium

7.1 Introduction

We have seen in chapter 5 that the propagation of surface plasmons can be visualized by detecting the fluorescence of dye molecules placed close to a metal surface. The two main disadvantages of this technique are bleaching of the dye, which limits quantitative and reproducible analysis, and the need for a spacer layer (in this case a polymer film) that is often not compatible with practical needs.

Several alternative imaging techniques exist, of which leakage radiation microscopy and PSTM are probably the most notable. However, these are mainly used to study the leaky surface plasmon modes propagating at a metal/air interface. A purely bound mode that has highest field concentrations at the large refractive index side of a metal film (a_b) does not produce leakage radiation. To detect such a wave efficiently with a near-field tip positioned at the air side of the film [82] a small film thickness is required. Imaging the bound LRSP mode (s_b) that can propagate along a metal film in a symmetric dielectric environment is even less straightforward. These LRSPs have received a lot of interest lately, especially at the 1.5 μm telecommunications wavelength [12, 13]. To measure the losses in LRSP waveguides, a cutback technique is generally used [10]. It would be interesting to develop a method to image the propagation and damping of these modes.

This chapter demonstrates the use of the fluorescence imaging technique to image infrared surface plasmons propagating at a Ag/glass interface. The problems of bleaching and spacer layers are overcome by using optically active erbium ions implanted in the glass at a well-defined distance to the Ag, that are acting as luminescent probes of the surface plasmon field intensity. The excitation of Er ions by surface plasmons generated with visible light was demonstrated in chapter 6. Here we study the propagation and damping of surface plasmons excited at 1.49 μm by two-dimensional imaging of the Er photoluminescence intensity at 1.53 μm using a confocal microscope.

We are interested in the mode propagating at the Ag/glass interface of a Ag film on a fused silica substrate (a_b). To excite this mode locally with a focused beam incident from the air side of the film, two methods are employed separately. First, SPs at the Ag/air interface are excited on a grating in an extended Ag film by illuminating it with a focused beam at the angle that allows first order grating coupling to the s_l mode. The grating period a is chosen such that second order coupling to the a_b mode is possible at the same angle of incidence, so that the modes at both interfaces can cross-couple on the grating, as discussed in section 3.3.1. Second, the a_b mode is excited by first-order diffraction by focusing the

incident beam on a subwavelength hole array in a Ag film at the proper angle to excite surface plasmons at the Ag/glass interface, as described in section 3.4.

7.2 Experimental

Fused silica substrates of 500 μm thickness (Suprasil 300, Heraeus) were implanted with Er ions at an average depth of 60 nm using 150 keV Er^+ ions at a fluence of $7 \cdot 10^{15}$ Er/cm^2. After annealing the samples in vacuum at 900°C, structured Ag films were fabricated as described in chapter 4. On the one hand, 46 nm deep gratings were formed in a 65 nm thick Ag film by thermally evaporating Ag directly on a substrate patterned with EBL and RIE. The pitch of the gratings was chosen to be 3.26 μm to satisfy equation 3.1. Using ellipsometry, the optical constants of the Ag film were determined (Fig. 4.2). Hole arrays connected to waveguides were fabricated in 96 nm thick Ag films deposited by electron-beam evaporation using a 4 nm thick Si adhesive layer. The pitch and hole size of these structures were varied to obtain maximum coupling to SPs. The hole arrays were connected to 115 μm long, 20 μm wide Ag stripes that can guide the excited surface plasmon beams.

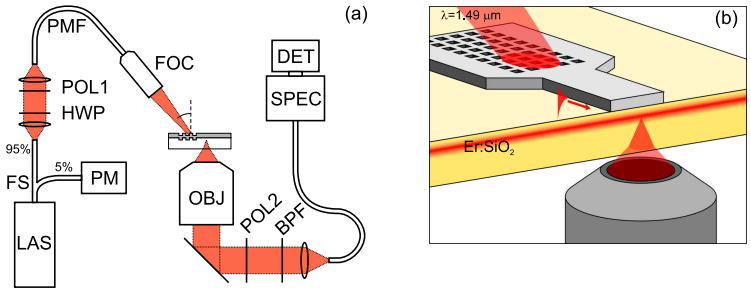

Figure 7.1: (a) Schematic of the setup used. LAS: 1.49 μm laser diode, FS: fiber splitter, PM: power meter, HWP: half wave plate, POL1: polarizer to control excitation polarization, PMF: polarization maintaining fiber, FOC: fiber focuser, OBJ: 20× objective, POL2: polarizer to select detected polarization, BPF: band-pass filter transmitting 1508-1556 nm, SPEC: spectrograph, DET: photodiode array detector. (b) Principle of the imaging technique.

A schematic of the setup used is displayed in Fig. 7.1(a). Excitation light of 1.49 μm from a 45 mW InGaAsP laser diode was coupled into a single mode polarization maintaining fiber after passing through a half wave plate and a polarizer, to select either *s*- or *p*-polarized excitation. The light was focused on the sample surface under a controllable angle with a fiber focuser, resulting in a spot with a full width at half maximum of 9.5 μm in the direction perpendicular to the plane of incidence. The angular distribution of the excitation beam has a Gaussian shape with a full width at half maximum of 6.1°. Light was collected from the substrate side of the sample with a 20× objective (Nikon, NA=0.4), and passed through a polarizer (with polarization direction perpendicular to the excitation polarization) and a bandpass filter transmitting wavelengths between 1508 and 1556 nm, to reduce the power of the 1.49 μm excitation light. Spectra were recorded by dispersing the reflected light with a spectrograph (Acton SpectraPro 2300i) onto a liquid nitrogen-cooled InGaAs photodiode array detector (Princeton Instruments OMA V). A homogeneous background of 500 counts/pixel due to dark current of the detector was measured and subtracted from the spectra. The sine of the angle of the incident beam with the surface normal was larger than the numerical aperture of the objective to avoid collection of the directly transmitted laser beam. However, due to scattering and diffraction at the Ag microstructures, a significant amount of 1.49 μm light was detected. A typical spectrum showing peaks attributed to laser scattering and Er emission is displayed in Fig. 7.2. The sample stage of the confocal microscope (Witec AlphaSNOM) was scanned, together with the excitation beam, with

respect to the collection objective to obtain a two-dimensional spectrally resolved map of the Er emission and pump scattering. A schematic of the excitation and detection of surface plasmons with these techniques is depicted in Fig. 7.1(b).

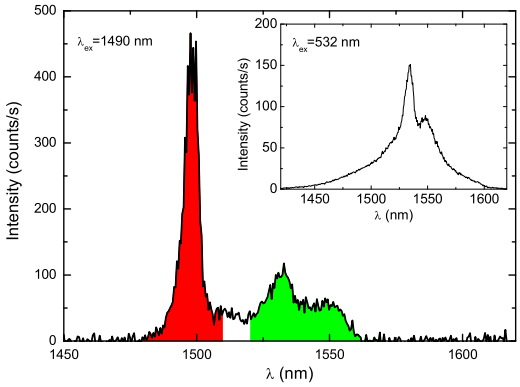

Figure 7.2: A typical spectrum collected with the setup described in the text with a 3 s acquisition time, showing scattered 1.49 μm laser light (red) and Er photoluminescence (green). The inset shows the Er photoluminescence spectrum for 532 nm excitation with a 60 s acquisition time, without the presence of a bandpass filter in the collection path.

7.3 Results and discussion

7.3.1 Surface plasmons on a cross-coupling grating

A grating with a pitch of 3.26 μm and large lateral dimensions fabricated in a 65 nm Ag film was illuminated as described above at an angle of 34° to allow excitation of both the s_l and the a_b mode, through first- and second-order grating coupling, respectively. For this grating pitch, the surface plasmon modes at opposing interfaces are cross-coupled on the grating, which is believed to cause efficient transfer of energy across the film [46–49]. Figure 7.3 shows confocal microscopy images of the intensity in a wavelength range centered around the laser wavelength (1480-1510 nm). For p-polarized excitation, the incident spot is clearly visible, together with a beam emerging from the excitation spot in the plane of incidence. The excitation spot observed when the pump is s-polarized has one fifth of the intensity of the p polarization case. For s-polarized excitation, a very weak beam is also observed (shown in the inset of Fig. 7.3(b)), with 0.035 times the intensity of the beam excited by p-polarized light.

The collected light originates from scattering at film imperfections and from grating diffraction, since unlike the directly transmitted excitation beam, the -1 and -2 diffraction orders transmitted into the glass are collected by the objective. This could explain the difference in intensity of the excitation spot for perpendicular polarizations.

The most plausible explanation for the observation of a clear beam for p-polarized excitation is that the incident light can couple to surface plasmons, that propagate for a certain distance across the grating, and that can lose part of their energy to diffraction into the detected -1 and -2 transmitted diffraction orders. We see that the surface plasmon beam is not scattered out at $x = 160$ μm in Fig. 7.3(a), which is attributed to the fact that at that position a few grating grooves are missing due to a fabrication error.

In this view, it would not be expected to see any of these effects for s-polarized excitation. The fact that a weak beam is nevertheless observed can be ascribed to the error in the

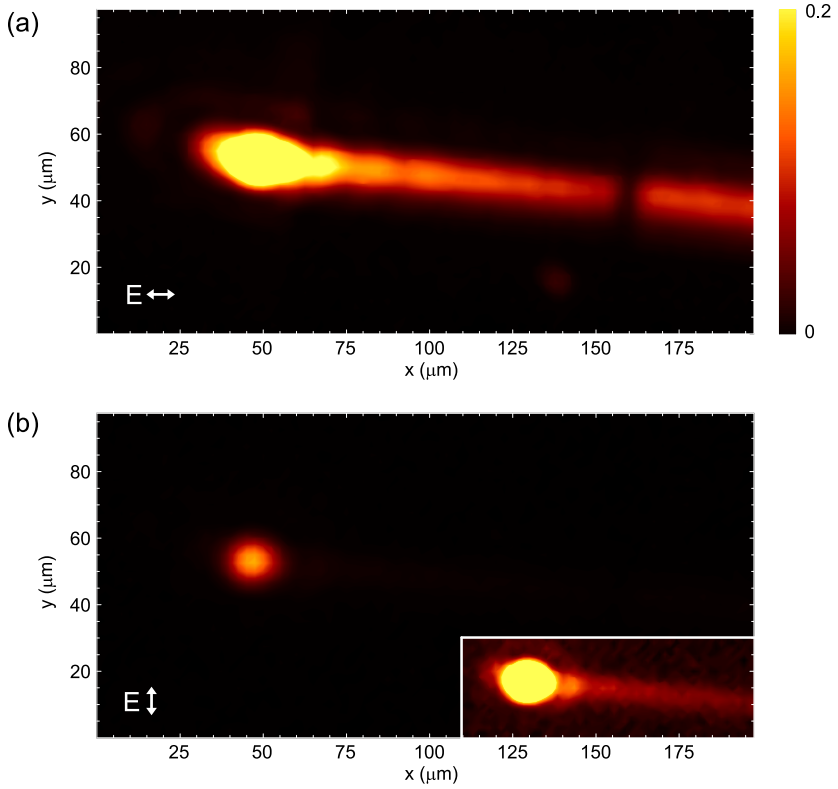

Figure 7.3: Confocal microscopy images of the intensity in the wavelength range of 1480-1510 nm, showing the focused excitation beam on an extended grating of 3.26 μm pitch. The plane of incidence is parallel to the x-axis, the grating grooves are parallel to the y-axis. (a) p-polarized excitation, the color scale was normalized to 0.2 times the maximum intensity. (b) s-polarized excitation, at the same scale as (a). The inset shows a detail of the same image with the color scale normalized to 0.1 times the maximum intensity in (b).

excitation polarization angle, which is comparable to the 2° deviation that would give rise to the measured intensity difference. However, we must note that another effect might play a role in the explanation: The beam could in principle also be ascribed to the scattering of a diffracted light beam travelling at a grazing angle close to the surface, because the focused excitation beam also contains angles that can be diffracted into such a diffraction order. Since we can calculate the fraction of energy coupled to surface plasmons and the energy diffracted into the grazing angle order for a particular angle of incidence as described in chapter 3, and because we know the angular distribution of the excitation beam, we can estimate that roughly two times more energy is used for surface plasmon excitation than for first order diffraction. Because furthermore most of the first order diffracted light propagates at an angle of 6° to the surface, we believe that scattering of this beam at surface corrugations would only be significant in the first few tens of micrometers.

If we suppose that both grazing angle diffracted light and surface plasmons are produced to a comparable degree, it might be possible for the two to interfere to produce a beating pattern in the intensity along the observed beam, from which the difference of the two wave vectors could be determined. Indeed, a small oscillatory pattern with a 16±2 μm period can be discerned in the first 40 μm of the intensity decay, that is shown as a red curve in Fig. 7.4. However, such a periodicity would arise from light with wave vector k_0 interfering with a surface plasmon with wave vector $1.09k_0$, instead of the expected $1.006k_0$ calculated for a 1.49 μm surface plasmon on this grating geometry.

7.3.2 Propagation lengths on a grating and on a smooth film

The excitation spot was placed close to the edge of the grating area, to launch surface plasmons propagating on the smooth film outside the grating. In this region Er luminescence was detected along the direction of the surface plasmon beam. Figure 7.4 shows the corresponding decay of luminescence between 1520 and 1570 nm with distance from the grating. In the absence of diffracting grooves, the intensity of the collected light around the laser wavelength, which is also shown in the figures, does not mimic the attenuation evident in the Er signal. Fitting an exponential decay to these Er data gives a $1/e$ propagation length of 78±6 μm. This length is considerably shorter than the propagation length on the grating, deduced from a cross section of Fig. 7.3 along the beam: fitting the decay of the diffracted laser light on the grating (the red curve in Fig. 7.4) yields a propagation length of 236±2 μm.

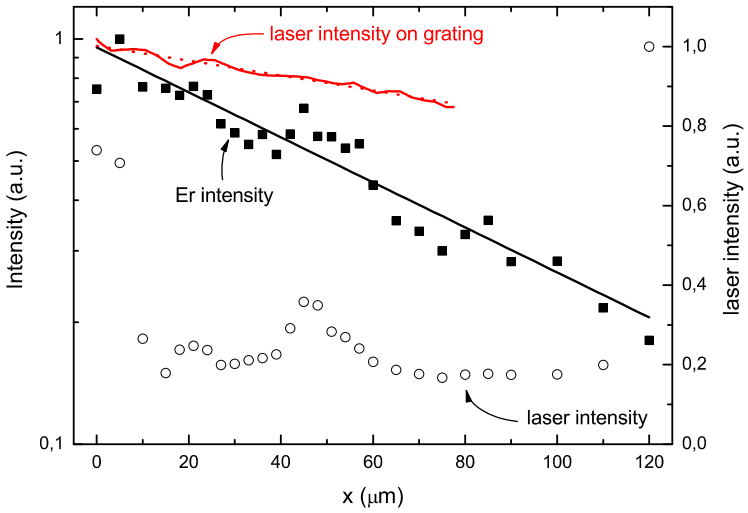

Figure 7.4: Er photoluminescence intensity and scattered laser intensity for varying distance from the grating edge. The red curve shows the scattered intensity along the beam on the grating in Fig 7.3(a) between $x = 70$ μm and $x = 150$ μm.

To interpret these results we have to compare the excitation and damping of the a_b and s_l modes. The theoretical propagation length of the a_b mode concentrated at the Ag/glass interface on a smooth film with the thickness and optical constants measured on the sample under study is 150 μm, and that of the s_l mode is 390 μm. Although both modes can be excited at the same time with this geometry, either through first or second order grating coupling, we have concluded in section 3.3.1 that the s_l mode is excited much more efficiently. It was seen from transmission calculations that a large part of the diffraction collected at the substrate side of the grating is expected to originate from diffraction of the s_l mode. Moreover, because both modes could in principle couple through the grating outside the region of excitation as well, their decay on the grating should be equal.

Outside the grating, the surface plasmon modes are not coupled, so their propagation lengths will be different in that region. By calculating the time-averaged Poynting vector of both modes, we can estimate the energy flux of the a_b mode at the position of the Er ions to be 3000 times as high as the energy flux of the s_b mode at that height below the film, when the modes are equally strong. Since we saw in section 3.3.1 that the s_b mode is excited only approximately 20 times more efficiently than the a_b mode, it is expected that the decay of Er luminescence with distance from the grating is governed by the damping of the a_b mode. This is supported by the observation that the propagation length fitted to the Er intensity *outside* the grating is smaller than the propagation length fitted to the diffracted radiation intensity *on* the grating.

It should be noted that the expected propagation length of the s_l mode on the grating given by reflection spectra calculations is 160 μm, which is shorter than the 240 μm observed. This discrepancy is still unexplained, and has to be confirmed by further measurements. It casts some doubt on the validity of determining SP propagation lengths by scattering, but one factor that might also play a role here is that the shape of the grooves is more rounded than the right-angle groove shape of the model, resulting in relatively smaller scattering than calculated.

7.3.3 Excitation of surface plasmons by hole arrays

Figure 7.5 shows the normal incidence transmission spectrum of a 96 nm thick Ag hole array with a pitch of 1.02 μm. Even though approximately 30% of the silver 'caps' were still on the holes (see section 4.3.3), distinct peaks are observed, that are generally believed to be related to the excitation of surface plasmons [52–57]. The peak at 1.12 μm is the combined effect of (1,0) excitation of SPs at the metal/air interface and (1,1) excitation of SPs at the metal/glass interface. The other transmission peak, centered around 1.48 μm, is attributed to the (1,0) excitation of surface plasmons at the metal/glass interface. We can make a rough estimation of the damping of the a_b mode on the hole array from the width of this peak. Neglecting other broadening effects, the corresponding propagation length would be 4-7 μm.

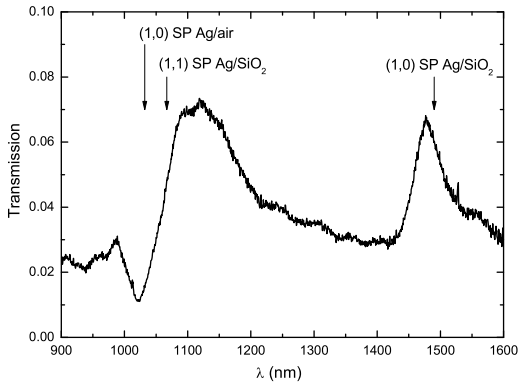

Figure 7.5: Normal incidence transmission spectrum of a subwavelength hole array with 1.02 μm pitch in a 96 nm Ag film on fused silica glass. Approximately 30% of the holes was covered with silver. The arrows indicate the wavelengths that would satisfy the simplified SP coupling condition 3.2 for normal incidence.

Considering the position of this peak for normal incidence, it is expected from equation 3.2 that for a 2 μm pitch, the a_b mode will be excited with 1.49 μm light at a 45° incident angle. Applying these conditions in the setup described above, SP beams were launched by such hole arrays into wide Ag stripes. A bright-field transmission microscopy image of the sample showing the hole array (with a few holes missing due to unsuccessful lift-off) and the 115 μm long, 20 μm wide Ag stripe is shown in Fig. 7.6. The images obtained from integrating the spectra collected on the Ag stripe around the laser wavelength (1480-1510 nm) and the Er emission (1520-1570 nm), as depicted in Fig. 7.2, are shown in Fig. 7.7 for both *p*- and *s*-polarized excitation. The outline of the rectangular stripe region, which starts at $x = 0$ μm, is indicated by the dashed lines. A clear SP beam is evident in the Er signal for *p* polarization, that is seen to be confined to the Ag stripe. Only a very weak beam is observed for *s*-polarized excitation, that can again be ascribed to the

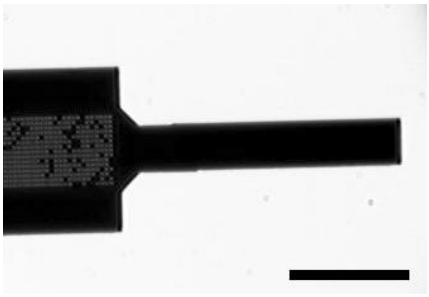

Figure 7.6: Transmission microscopy image of the Ag microstructure that was studied. The scale bar is 50 μm.

instrumental error in the excitation polarization angle. The beam cannot be discerned from the intensity of the laser wavelengths (Fig. 7.7(b)), which seems to show only scattering at the edges of the structure. Although surface plasmons will definitely scatter to radiation at the end of the waveguide [16], it is not possible to attribute the large laser intensity at the end of the waveguide completely to surface plasmon scattering, because it is also visible for s-polarized excitation, albeit with a somewhat lower intensity. It is probably partly caused by scattering of incident and diffracted laser light at a fabrication-related defect.

7.3.4 Propagation of the a_b mode on a metal stripe

Because the Ag film is optically thick, and the periodicity of the hole array was specifically designed for excitation of the a_b mode, we can assume that Er ions are only excited by the a_b surface plasmon mode, or possibly by diffracted light travelling in the glass at a glancing angle to the Ag/glass interface.

In Figure 7.8 the intensity of the Er signal along the center of the beam that was observed for p polarization is plotted as black squares. After 10 μm, the intensity is seen to be attenuated with increasing distance. The $1/e$ length of this decrease is approximately 85 μm, but depends on the fitted range. When fitting Gaussian curves to cross sections of the beam, we can see that the beam width varies, and actually reaches a minimum at $x = 70$ μm (shown as blue circles in Fig. 7.8). It could have been possible that the excitation beam was focused just below the sample surface, so that also the (diffracted) surface plasmon beam experienced a focussing effect, but it may also be the result of an interaction of the SP with the side of the stripe. It is thus more accurate to estimate the propagation length of the SP mode from the decrease of the area under cross sections of the beam for increasing x. These values are displayed in Fig. 7.8 as red triangles. The red line is a fit to all data points on the stripe, with a $1/e$ length of 60 ± 2 μm. It is clear that especially at the start of the waveguide the decay is not a perfect exponential; it might be possible that the Er ions are also excited by diffracted light. Fitting an exponential decay for $x > 37$ μm gives a propagation length of 76 ± 1 μm, displayed in Fig. 7.8 as the red dotted line. Observing the decay along longer distances is required to gain better insight in the character of the damping.

The theoretical propagation length of the a_b mode in a 96 nm Ag film on 4 nm Si on a fused silica substrate is 135 nm, obtained from dipole power dissipation calculations using the dielectric constants displayed in Fig. 4.2.2. The observed $1/e$ length of the Er luminescence intensity decay suggests that damping due to scattering at surface roughness plays a role as well.

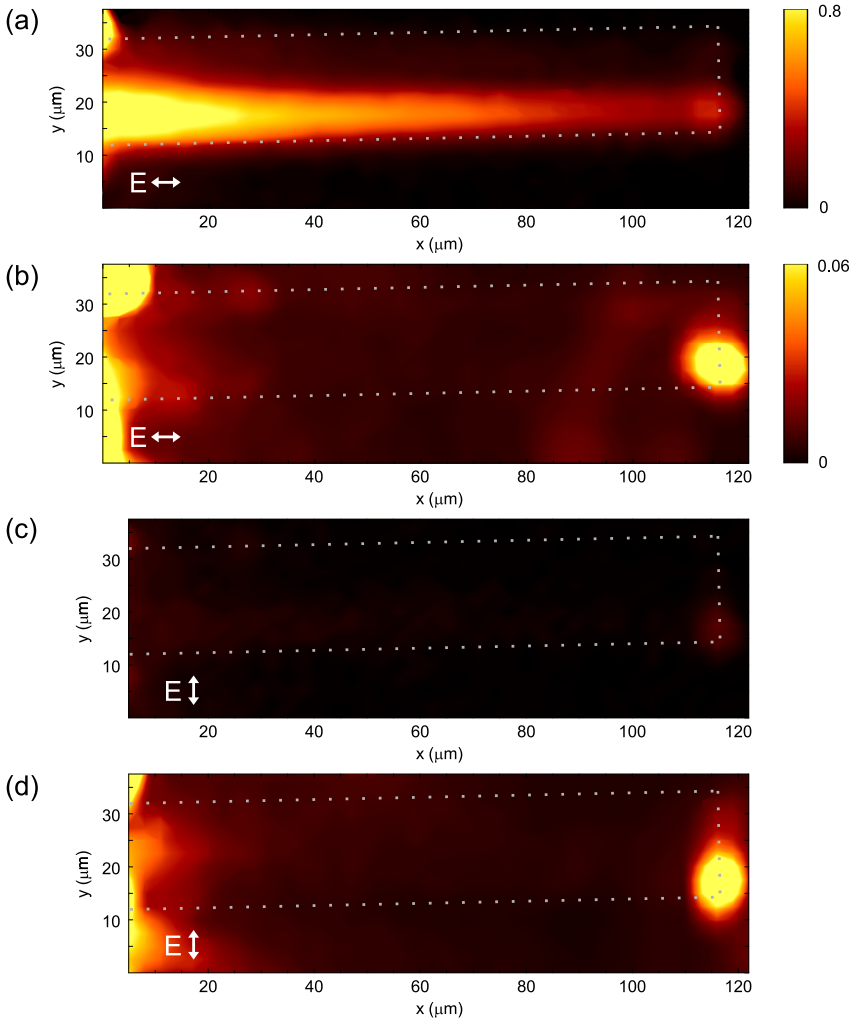

Figure 7.7: (a) and (c): Confocal images of the Er photoluminescence intensity between 1520 and 1570 nm, for *p*- and *s*-polarized excitation on a hole array located to the left of the field of view. The plane of incidence is parallel to the x-axis. (b) and (d): Images of the intensity around the laser wavelength between 1480 and 1510 nm, taken from the same measurements as (a) and (c). The color scale of (a) is normalized to 0.8 times the maximum intensity, and that of (b) is normalized to 0.06 times the maximum intensity. (c) and (d) are at the same color scale as (a) and (b), respectively.

7.4 Conclusions and outlook

We have demonstrated the use of implanted erbium ions to image the propagation of infrared surface plasmons, that were launched along the Ag/glass interface of a Ag film using gratings and arrays of subwavelength holes. The propagation lengths of these modes have been obtained by analyzing the decay of Er photoluminescence intensity along the observed surface plasmon beams. It will be necessary to study this behavior along longer distances, to be able to observe exponential decay of the intensity over multiple orders of magnitude and to discern surface plasmon excitation from diffraction effects. Furthermore, it would be desirable to increase the control over the excitation polarization, and to reduce the intensity of the laser wavelengths compared to that of the Er luminescence, to be able to collect Er photoluminescence spectra on gratings and hole arrays. Cross-coupling gratings might

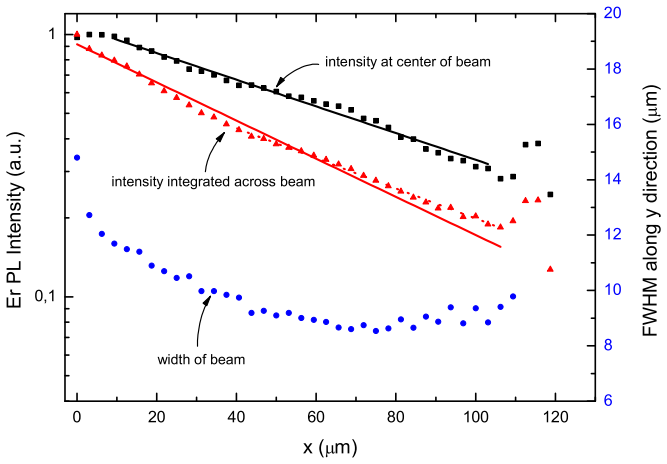

Figure 7.8: Er photoluminescence intensity for varying distance along the beam observed in Fig. 7.7(a), showing the intensity at the center of the beam, the intensity integrated over a cross-section of the beam, and the width of the beam. Lines are exponential fits to different data sets.

allow transfer of energy between the modes at opposing interfaces. The dependence of the efficiency of this process on grating parameters and film thickness could be studied in more detail both theoretically and experimentally. Finally, the excitation efficiency of surface plasmons on hole arrays might be greatly enhanced by changing the hole size and shape [62, 63].

This imaging technique is useful to study the propagation and damping of infrared surface plasmons bound to a metal/dielectric interface at the important telecommunications wavelength of 1.5 μm, for instance the long-ranging modes in thin metal films in a symmetric dielectric environment. It can be employed to locally probe the surface plasmon field intensity at positions in plasmonic structures that are not readily accessible with other imaging techniques.

Bibliography

[1] A. Polman, *Erbium implanted thin film photonic materials*, J. Appl. Phys. **82**, 1 (1997).

[2] H. Raether, *Surface plasmons*, Springer-Verlag, Berlin Heidelberg, 1988.

[3] W. L. Barnes, A. Dereux, and T. W. Ebbesen, *Surface plasmon subwavelength optics*, Nature **424**, 824 (2003).

[4] H. Ditlbacher, J. R. Krenn, N. Felidj, B. Lamprecht, G. Schider, M. Salerno, A. Leitner, and F. R. Aussenegg, *Fluorescence imaging of surface plasmon fields*, Appl. Phys. Lett. **80**, 404 (2002).

[5] E. Palik, editor, *Handbook of optical constants of solids*, Academic Press, Inc., New York, 1985.

[6] *Heraeus quarz glass technical data sheet*, www.heraeus-quarzglass.com, 2005.

[7] H. Ditlbacher, J. R. Krenn, A. Hohenau, A. Leitner, and F. R. Aussenegg, *Efficiency of local light-plasmon coupling*, Appl. Phys. Lett. **83**, 3665 (2003).

[8] D. Sarid, *Long-range surface-plasma waves on very thin metal films*, Phys. Rev. Lett. **47**, 1927 (1981).

[9] R. Charbonneau, P. Berini, E. Berolo, and E. Lisicka-Shrzek, *Experimental observation of plasmon polariton waves supported by a thin metal film of finite width*, Opt. Lett. **25**, 844 (2000).

[10] T. Nikolajsen, K. Leosson, I. Salakhutdinov, and S. Bozhevolnyi, *Polymer-based surface-plasmon-polariton stripe waveguides at telecommunication wavelengths*, Appl. Phys. Lett. **82**, 668 (2003).

[11] J. J. Burke, G. I. Stegeman, and T. Tamir, *Surface-polariton-like waves guided by thin, lossy metal films*, Phys. Rev. B **33**, 5186 (1986).

[12] T. Nikolajsen, K. Leosson, and S. Bozhevolnyi, *Surface plasmon polariton based modulators and switches operating at telecom wavelengths*, Appl. Phys. Lett. **85**, 5833 (2004).

[13] R. Charbonneau, N. Lahoud, G. Mattiussi, and P. Berini, *Demonstration of integrated optics elements based on long-ranging surface plasmon polaritons*, Opt. Expr. **13**, 977 (2005).

[14] P. Dawson, F. de Fornel, and J-P. Goudonnet, *Imaging of surface plasmon propagation and edge interaction using a photon scanning tunneling microscope*, Phys. Rev. Lett. **72**, 2927 (1994).

[15] J. R. Krenn, R. Wolf, A. Leitner, and F. R. Aussenegg, *Near-field optical imaging the surface plasmon fields of lithographically designed nanostructures*, Opt. Commun. **137**, 46 (1997).

[16] J.-C. Weeber, J. R. Krenn, A. Dereux, B. Lamprecht, Y. Lacroute, and J. P. Goudonnet, *Near-field observation of surface plasmon polariton propagation on thin metal stripes*, Phys. Rev. B **64**, 045411 (2001).

[17] S. I. Bozhevolnyi, J. Erland, K. Leosson, P. M. W. Skovgaard, and J. M. Hvam, *Waveguiding in surface plasmon polariton band gap structures*, Phys. Rev. Lett. **86**, 3008 (2001).

[18] B. Lamprecht, J. R. Krenn, G. Schider, H. Ditlbacher, M. Salerno, N. Felidj, A. Leitner, and F. R. Aussenegg, *Surface plasmon propagation in microscale metal stripes*, Appl. Phys. Lett. **79**, 51 (2001).

[19] B. Hecht, H. Bielefeldt, L. Novotny, Y. Inouye, and D. W. Pohl, *Local excitation, scattering, and interference of surface plasmons*, Phys. Rev. Lett. **77**, 1889 (1996).

[20] A. Bouhelier, Th. Huser, H. Tamaru, H.-J. Güntherodt, D. W. Pohl, F. I. Baida, and D. Van Labeke, *Plasmon optics of structured silver films*, Phys. Rev. B **63**, 155404 (2001).

[21] A. Hohenau, J. R. Krenn, A. L. Stepanov, A. Drezet, H. Ditlbacher, B. Steinberger, A. Leitner, and F. R. Aussenegg, *Dielectric optical elements for surface plasmons*, Opt. Lett. **30**, 893 (2005).

[22] H. Ditlbacher, J. R. Krenn, G. Schider, A. Leitner, and F. R. Aussenegg, *Two-dimensional optics with surface plasmon polaritons*, Appl. Phys. Lett. **81**, 1762 (2002).

[23] B. Prade, J. Y. Vinet, and A. Mysyrowicz, *Guided optical waves in planar heterostructures with negative dielectric constant*, Phys. Rev. B **44**, 13556 (1991).

[24] Fuzi Yang, J. R. Sambles, and G. W. Bradberry, *Long-range surface modes supported by thin films*, Phys. Rev. B **44**, 5855 (1991).

[25] T. Tamir and A. A. Oliner, *The spectrum of electromagnetic waves guided by a plasma layer*, Proc. IEEE (London) **110**, 317 (1963).

[26] P. Berini, *Plasmon-polariton waves guided by thin lossy metal films of finite width: Bound modes of asymmetric structures*, Phys. Rev. B **63**, 125417 (2001).

[27] J. A. Dionne, L. A. Sweatlock, H. A. Atwater, and A. Polman, *Planar metal plasmon waveguides: frequency-dependent dispersion, propagation, localization, and loss beyond the free electron-model*, Phys. Rev. B, in press (2005).

[28] M. A. Born and E. Wolf, *Principles of optics*, Pergamon Press, London New York Paris Los Angeles, 1959.

[29] G. I. Stegeman, J. J. Burke, and D. G. Hall, *Surface-polaritonlike waves guided by thin, lossy metal films*, Opt. Lett. **8**, 383 (1983).

[30] J.-C. Weeber, Y. Lacroute, and A. Dereux, *Optical near-field distributions of surface plasmon waveguide modes*, Phys. Rev. B **68**, 115401 (2003).

[31] R. Zia, M. D. Selker, and M. L. Brongersma, *Leaky and bound modes of surface plasmon waveguides*, Phys. Rev. B **71**, 165431 (2005).

[32] K. L. Kliewer and R. Fuchs, *Optical modes of vibration in an ionic crystal slab including retardation. I. Nonradiative region*, Phys. Rev. **144**, 495 (1966).

[33] L. Wendler and R. Haupt, *Long-range surface plasmon-polaritons in asymmetric layer structures*, J. Appl. Phys. **59**, 3289 (1986).

[34] P. Berini, *Plasmon-polariton modes guided by a metal film of finite width*, Opt. Lett. **24**, 1011 (1999).

[35] G. W. Ford and W. H. Weber, *Electromagnetic interactions of molecules with metal surfaces*, Phys. Rep. **113**, 195 (1984).

[36] J. Kalkman, L. Kuipers, A. Polman, and H. Gersen, *Coupling of Er ions to surface plasmons on Ag*, Appl. Phys. Lett. **86**, 041113 (2005).

[37] R. Petit, editor, *Electromagnetic theory of gratings*, Springer-Verlag, Berlin, 1980.

[38] I. R. Hooper and J. R. Sambles, *Surface plasmon polaritons on thin-slab metal gratings*, Phys. Rev. B **67**, 235404 (2003).

[39] I. Pockrand and H. Raether, *Surface plasma oscillations in silver films with wavy surface profiles: A quantitative experimental study*, Opt. Commun. **18**, 395 (1976).

[40] H. Raether, *Dispersion relation of surface plasmons on gold- and silver gratings*, Opt. Commun. **42**, 217 (1982).

[41] S. H. Zaidi, M. Yousaf, and S. R. J. Brueck, *Grating coupling to surface plasma waves. I. First-order coupling*, J. Opt. Soc. Am. B **8**, 770 (1991).

[42] A. C. R. Pipino and G. C. Schatz, *Surface-profile dependence of photon-plasmon-polariton coupling at a corrugated silver surface*, J. Opt. Soc. Am. B **11**, 2036 (1994).

[43] B. Gralak, M. de Dood, G. Tayeb, S. Enoch, and D. Maystre, *Theoretical study of photonic band gaps in woodpile crystals*, Phys. Rev. E **67**, 066601 (2003).

[44] L. Li, *A modal analysis of lamellar diffraction gratings in conical mountings*, J. Mod. Opt. **40**, 553 (1993).

[45] U. Schröter and D. Heitmann, *Grating couplers for surface plasmons excited on thin metal films in the Kretschmann-Raether configuration*, Phys. Rev. B **60**, 4992 (1999).

[46] R. W. Gruhlke, W. R. Holland, and D. G. Hall, *Surface-plasmon cross coupling in molecular fluorescence near a corrugated thin metal film*, Phys. Rev. Lett. **56**, 2838 (1986).

[47] D. K. Gifford and D. G. Hall, *Extraordinary transmission of organic photoluminescence through an otherwise opaque metal layer via surface plasmon cross coupling*, Appl. Phys. Lett. **80**, 3679 (2002).

[48] S. Wedge, I. R. Hooper, I. Sage, and W. L. Barnes, *Light emission through a corrugated metal film: The role of cross-coupled surface plasmon polaritons*, Phys. Rev. B **69**, 245418 (2004).

[49] S. Wedge and W. L. Barnes, *Surface plasmon-polariton mediated light emission through thin metal*

films, Opt. Expr. **12**, 3673 (2004).

[50] H. J. Lezec, A. Degiron, E. Devaux, R. A. Linke, L. Martin-Moreno, F. J. Garcia-Vidal, and T. W. Ebbesen, *Surface plasmon propagation in microscale metal stripes*, Science **297**, 820 (2002).

[51] J. A. Porto, F. J. Garca-Vídal, and J. B. Pendry, *Transmission resonances on metallic gratings with very narrow slits*, Phys. Rev. Lett. **83**, 2845 (1999).

[52] T. W. Ebbesen, H. J. Lezec, H. F. Ghaemi, and T. Thio, *Extraordinary optical transmission through sub-wavelength hole arrays*, Nature **391**, 667 (1998).

[53] H. F. Ghaemi, T. Thio, D. E. Grupp, T. W. Ebbesen, and H. J. Lezec, *Surface plasmons enhance optical transmission through subwavelength holes*, Phys. Rev. B **58**, 6779 (1998).

[54] T. J. Kim, T. Thio, T. W. Ebbesen, D. E. Grupp, and H. J. Lezec, *Control of optical transmission through metals perforated with subwavelength hole arrays*, Opt. Lett. **24**, 256 (1999).

[55] D. E. Grupp, H. J. Lezec, T. W. Ebbesen, K. M. Pellerin, and T. Thio, *Crucial role of metal surface in enhanced transmission through subwavelength apertures*, Appl. Phys. Lett. **77**, 1569 (2000).

[56] A. Krishnan, T. Thio, T. J. Kim, H. J. Lezec, T. W. Ebbesen, P. A. Wolff, P. A. Wolff, J. Pendry, L. Martin-Moreno, and F. J. Garcia-Vidal, *Evanescently coupled resonance in surface plasmon enhanced transmission*, Opt. Commun. **200**, 1 (2001).

[57] W. L. Barnes, W. A. Murray, J. Dintinger, E. Devaux, and T. W. Ebbesen, *Surface plasmon polaritons and their role in the enhanced transmission of light through periodic arrays of subwavelength holes in a metal film*, Phys. Rev. Lett. **92**, 107401 (2004).

[58] D. S. Kim, S. C. Hohng, V. Malyarchuk, Y. C. Yoon, Y. H. Ahn, K. J. Yee, J. W. Park, J. Kim, Q. H. Park, and C. Lienau, *Microscopic origin of surface-plasmon radiation in plasmonic band-gap nanostructures*, Phys. Rev. Lett. **91**, 143901 (2003).

[59] E. Devaux, T. W. Ebbesen, J.-C. Weeber, and A. Dereux, *Launching and decoupling surface plasmons via micro-gratings*, Appl. Phys. Lett. **83**, 4936 (2003).

[60] D. Egorov, B. S. Dennis, G. Blumberg, and M. I. Haftel, *Two-dimensional control of surface plasmons and directional beaming from arrays of subwavelength apertures*, Phys. Rev. B **70**, 033404 (2004).

[61] A. Degiron, H. J. Lezec, W. L. Barnes, and T. W. Ebbesen, *Effects of hole depth on enhanced light transmission through subwavelength hole arrays*, Appl. Phys. Lett. **81**, 4327 (2002).

[62] K. J. K. Koerkamp, S. Enoch, F. B. Segerink, N. F. van Hulst, and L. Kuipers, *Strong influence of hole shape on extraordinary transmission through periodic arrays of subwavelength holes*, Phys. Rev. Lett. **92**, 183901 (2004).

[63] K. L. van der Molen, F. B. Segerink, and N. F. van Hulst, *Influence of hole size on the extraordinary transmission through subwavelength hole arrays*, Appl. Phys. Lett. **85**, 4316 (2004).

[64] C. A. Neugebauer, *Condensation, nucleation and growth of thin films*, in *Handbook of thin film technology*, edited by L. I. Maissel and R. Glang, McGraw-Hill, New York, 1970.

[65] H. K. Pulker, *Coatings on glass*, Elsevier, Amsterdam, 1984.

[66] M. J. Rost, D. A. Quist, and J. W. M. Frenken, *Grains, growth, and grooving*, Phys. Rev. Lett. **91**, 026101 (2003).

[67] K. E. Harris and A. H. King, *Localized texture formation and its detection in polycrystalline thin films of gold*, in *Mat. Res. Soc. Symposium Proc.*, edited by S. M. Yalisove, C. V. Thompson, and D. J. Eaglesham, volume 317, page 425, 1994.

[68] C. C. Wong, H. I. Smith, and C. V. Thompson, *Surface-energy-driven secondary grain growth in thin Au films*, Appl. Phys. Lett. **48**, 335 (1986).

[69] R. W. Cahn, *Recovery and recrystallization*, in *Physical Metallurgy*, edited by R. W. Cahn and P. Haasen, Elsevier, Amsterdam, 1983.

[70] P. B. Johnson and R. W. Christy, *Optical constants of the noble metals*, Phys. Rev. B **6**, 4370 (1972).

[71] C. Reale, *Optical constants of vacuum deposited thin metal films in the near infrared*, Infrared Phys. **10**, 173 (1970).

[72] J. A. Sánchez-Gil and A. A. Maradudin, *Near-field and far-field scattering of surface plasmon polaritons by one-dimensional surface defects*, Phys. Rev. B **60**, 8359 (1999).

[73] P. Andrew and W. L. Barnes, *Molecular fluorescence above metallic gratings*, Phys. Rev. B **64**, 125405 (2001).

[74] W. Knoll, M. R. Philpott, J. D. Swalen, and A. Girlando, *Emission of light from Ag metal gratings coated with dye monolayer assemblies*, J. Chem. Phys. **75**, 4795 (1981).

[75] J. S. Batchelder, A. H. Zewail, and T. Cole, *Luminescent solar concentrators. 2: Experimental and theoretical analysis of their possible efficiencies*, Appl. Opt. **20**, 3733 (1981).

[76] J. Kalkman, C. Strohhöfer, B. Gralak, and A. Polman, *Surface plasmon polariton modified emission of erbium in a metallodielectric grating*, Appl. Phys. Lett. **83**, 30 (2003).

[77] J. F. Ziegler, J. P. Biersack, and U. Littmark, *The stopping and range of ions in solids*, Pergamon Press, New York, 1985.

[78] M. J. A. de Dood, J. Knoester, and A. Polman, *Förster transfer and the local optical density of states in erbium-doped silica*, Phys. Rev. B **71**, 115102 (2005).

[79] E. Snoeks, G. N. van den Hoven, A. Polman, B. Hendriksen, M. B. J. Diemeer, and F. Priolo, *Cooperative upconversion in erbium-implanted soda-lime silicate glass optical waveguides*, J. Opt. Soc. Am. B **12**, 1468 (1995).

[80] F. L. Pedrotti and L. S. Pedrotti, *Introduction to optics*, Prentice-Hall, 1993.

[81] E. Hecht, *Optics*, Addison Wesley, San Francisco, 4th edition, 2002.

[82] J. Seidel, F. I. Baida, L. Bischoff, B. Guizal, S. Grafström, D. Van Labeke, and L. M. Eng, *Coupling between surface plasmon modes on metal films*, Phys. Rev. B **69**, 121405 (2004).

Acknowledgements

Without the help of many people this work would not have been possible. First and foremost, I would like to thank Albert Polman for his enthusiasm and for making so many things possible. I am looking forward to enjoying more of your inspirational supervision in the future. Thanks to all the people in the Photonic Materials group: Jeroen Kalkman and Hans Mertens for all their skills and knowledge, Jan van der Elsken, Anna Tchebotareva for helping me with the microscope, Joan Penninkhof, Martien den Hertog, René de Waele, Timon van Wijngaarden, Martin Kuttge, Sébastien Bidault, Rob van Loon, and the guests Denise Krol, Harry Atwater and his students. I have learned a lot from you all, and you made this year especially enjoyable. Thanks also to Kobus Kuipers and the students in his group, for interesting work discussions and coffee breaks. The people in the design department, the workshop and other supporting groups at AMOLF are acknowledged for their nice and efficient work. I would especially like to thank Chris Rétif for getting me started with fabrication and for all the help afterwards. Thanks to Boris Gralak for letting me use your code to calculate grating diffraction and for welcoming me in Marseille.

A big thanks goes to my parents for making my studies possible and for always believing in me, but above all, I would like to thank Kiki for all your support and so much more.